ON THE ACCURACY OF ESTIMATING INPUT IMPEDANCE OF PROBE-FED AIR-SUBSTRATE MICROSTRIP PATCH ANTENNAS USING THE THEORY OF CHARACTERISTIC MODES

BY

BRIAN B. GIBBONS

THESIS

Submitted in partial fulfillment of the requirements
for the degree of Master of Science in Electrical and Computer Engineering
in the Graduate College of the
University of Illinois at Urbana-Champaign, 2014

Urbana, Illinois

Adviser:

Professor Jennifer T. Bernhard

ABSTRACT

Two different techniques based on the theory of characteristic modes are developed to estimate the input impedance of air-substrate, coaxial probe-fed, microstrip patch antennas with arbitrarily shaped patches. Such an antenna with an L-shaped patch is fabricated and experimentally measured, and a case study performed comparing the accuracy of the two methods. The results of both methods require a downward frequency scaling on the order of 8 % to better agree with experiment, attributable to losses in the real-world materials. The simpler method (the virtual probe model) is shown to provide good input resistance predictions, but the input reactance is shown to require compensation in the form of series inductance and capacitance. The more involved method (the wire probe model) is demonstrated to provide both good input resistance and reactance estimates with only a frequency scaling. The results and conclusions of this case study are then used to draw implications for future work involving application of the theory of characteristic modes to antenna feeds.

To my parents, for their love and support.

ACKNOWLEDGMENTS

First and foremost, I would like to thank my adviser, Professor Jennifer Bernhard, for her continual help, useful insights, kind encouragements, and willingness to pursue interesting and complicated topics. The focus of this thesis at times bordered on being too broad or too complicated for a single master's thesis to reasonably cover; her help narrowing it down to a "bite-sized" piece of the larger problem of antenna feeding and feed modeling made this thesis possible.

I would also like to thank the members, both past and present, of Professor Bernhard's antenna research group for many helpful and interesting conversations. In particular, conversations with Kurt Schab, Nikki Bohannon, and Matt W. Young were instrumental in clarifying important topics and issues that arose throughout the development of this work.

Thanking the multitude of teachers, mentors, and professors that have taught and guided my education over the years would result in a lengthy and by no means exhaustive list, too long to detail here. A key individual I would especially like to thank is Professor Frank Merat: his course on electromagnetics is what introduced me to this field and ultimately led me to pursue the study of antenna design in graduate school. A second crucial individual is my father: his passion for and understanding of electrical engineering are largely what influenced me to likewise study electrical engineering. To all the rest of those who've helped me along the way, a simple "thank you" will just have to suffice.

TABLE OF CONTENTS

LIST OF ABBREVIATIONS

CM	Characteristic (Current) Mode
MSA	Microstrip (Patch) Antenna
PEC	Perfect Electrical Conductor
RF	Radio Frequency
TCM	Theory of Characteristic Modes

SYMBOLS AND NOTATION

j	The imaginary unit, $\sqrt{-1}$
λ	1 wavelength
δ_{mn}	The Kronecker delta, defined as $$\delta_{mn} = \begin{cases} 1, & m = n \\ 0, & m \neq n \end{cases}$$
$\mathrm{Re}[a]$	Denotes taking the real component of a
$\mathrm{Im}[a]$	Denotes taking the imaginary component of a
$\vec{J}$	An overhead arrow denotes a column vector
$\mathbf{Z}$	Boldface type denotes a matrix
$\mathbf{Z}^T$	A superscript T denotes a matrix or vector transpose
$\mathbf{Z}^*$	A superscript $*$ denotes a matrix or vector complex conjugate
$\mathbf{Z}^H$	A superscript H denotes a matrix or vector conjugate-transpose, *i.e.* $\mathbf{Z}^H = (\mathbf{Z}^*)^T = (\mathbf{Z}^T)^*$

CHAPTER 1

INTRODUCTION

Antennas occupy a special place within electrical engineering. They are among the oldest applications of this field, yet are neither outdated nor made obsolete by newer technologies. In fact, the modern-day trend toward an increasingly interconnected, yet wireless, society has only led to the proliferation of antennas. The RF and microwave regions of the electromagnetic spectrum, once seen as an expansive medium for communication and detection, are now heavily congested and viewed as a scarce natural resource as electromagnetic radiation finds more and more consumer, industrial, scientific, and military applications.

Given its age and these recent developments, the field of antenna engineering has undergone considerable change over the past 120 years. The advent of the digital computer (and its own rapid development) has arguably had the greatest impact; the iterative design process inherent in engineering that once required considerable fabrication and measurement time and cost is now greatly accelerated by computer simulations and tools. Nevertheless, with the increasing ease and low cost of using computers for antenna analysis and design comes a particular danger: that of uninformed, brute-force design approaches.

A perennial problem within antenna engineering is that of antenna feed placement. Although most structures will radiate to some extent regardless of feed position, careful design of this parameter is typically crucial for good performance of the antenna (measured by any number of metrics). Since the location of the feed can greatly influence the currents excited on the antenna, it also influences how the antenna interacts with whatever system it is connected to. One parameter borrowed from circuit theory that is used when measuring this interaction is input impedance. Knowledge and control of this parameter are desirable, as its value sets how effectively an antenna may transfer energy to and/or from its associated system. In most cases,

the antenna's input impedance must be close to some prescribed value derived from the connected system's own input impedance (*e.g.*, equal to the complex conjugate). When the antenna's input impedance deviates significantly from this desired value, it can be corrected by means of a matching network. Unfortunately, such networks incur additional power loss, take up more space, add more cost, and may also reduce operable bandwidth. It is therefore desirable, whenever possible, to adjust the antenna feed position for an appropriate input impedance.

Determination of antenna input impedance as a function of position may be done in a number of ways. For well-studied antenna structures, years of research and experimentation have yielded design formulas obtained either empirically or through theoretical modeling, *e.g.*, the rectangular microstrip patch antenna. Such formulas often offer a certain degree of insight into the behavior of the antenna. This approach, while highly desirable, has the downside that it can never encompass all possible antenna designs; indeed, this method is frequently limited just to antennas of canonical shapes. A second method for input impedance determination, more recently enabled by computers, is brute-force simulation. An antenna will be designed and simulated with a given feed location to determine the input impedance. The feed position will then be changed and the simulations rerun. This may be repeated for a set of positions or until a target impedance is reached. This approach has the disadvantages of offering less intuition into the antenna behavior and being much more demanding computationally. The third approach, taken here, is largely a hybrid of the two prior approaches. Using computational electromagnetics methods, antenna input impedance as a function of feed position is obtained through the numerical solution of an eigenvalue problem. Such an approach has the benefits of both being more generalizable to a greater class of antenna geometries and offering a degree of insight into the antenna behavior, all without the high computational cost of a brute-force approach.

In this thesis, a method for estimating the input impedance of coaxial probe-fed, air-substrate microstrip patch antennas will be developed from eigensolutions to the theory of characteristic modes. Background on this theory will be provided in Chapter 2 and the two input impedance estimation methods using this theory will be developed in Chapter 3. Chapter 4 will provide an analysis of the two methods through the use of a case study, com-

paring results with experimental data and a standard, commercial electromagnetic solver. Finally, important results and future work will be discussed in Chapter 5.

CHAPTER 2

BACKGROUND

The theory of characteristic modes provides the underlying mathematics utilized in this thesis for the estimation of antenna input impedance. Its origin, derivation, and implementation will be briefly discussed, followed by its relevant important properties and extension to multiple frequencies. Following this, methods for estimating antenna input impedance will be discussed with a primary focus on microstrip patch antennas.

2.1 Theory of Characteristic Modes

The theory of characteristic modes (TCM) was initially formulated in Garbacz's 1968 Ph.D. dissertation [1]; Garbacz and Turpin subsequently published an article on it in 1971 [2]. It was developed for a more intuitive analysis of scattering by perfectly electrically conducting (PEC) scattering objects near resonance, as compared to existing numeric approaches that offered little intuition into the nature of the problem at hand. TCM in practice is closely tied to the method of moments, a well-established frequency domain method for numerically solving steady-state electromagnetic scattering and radiation problems. Consequently, a basic TCM analysis is a steady-state solution at a single frequency.

At its heart, TCM takes the scattering operator for a PEC object and constructs an infinite, orthogonal set of far field electric field modal solutions that diagonalize the scattering operator. Associated with each of these orthogonal far fields is a surface electric current on the scatterer that would radiate the far field mode, termed a characteristic (current) mode (CM). TCM was recast by Harrington and Mautz in 1971 [3] into the form typically used nowadays, which defines a generalized eigenvalue problem and tends to focus more on the CMs and less on the scattered far fields. Specific details in a subsequent

paper [4] explain how to implement the eigenproblem in a finitely discretized space via a generalized *matrix* eigenvalue problem. Although it will not be pursued here, TCM may be generalized to magneto-dielectric bodies using volume current densities [5] or equivalent surface current densities [6]; such implementations are more complicated and currently not well explored.

2.1.1 Overview of TCM for PEC Structures

Calculation of the CMs of a PEC structure via Harrington and Mautz's approach [3], [4] begins by first obtaining the structure's impedance matrix at the given frequency of interest. This matrix, also known as the $\mathbf{Z}$ matrix, is a finite discretization of the object's scattering operator; intuitively, it relates a surface tangential electric current density $\vec{J}$ over the scatterer to the incident electric field $\vec{E}^i$ tangential to the surface that excites the current:

$$\vec{E}^i = \mathbf{Z}\vec{J} \tag{2.1}$$

The $\mathbf{Z}$ matrix is usually obtained from a method of moments code. In this thesis, the commercial solver FEKO [7] was used to generate these matrices. For the vectors defined over the surface of the object, one may approximate and discretize these quantities with a finite, weighted sum of basis functions. FEKO, for example, defaults to using RWG basis functions [8] for these purposes. These discrete expansions are then representable as finite-dimensional column vectors containing the coefficients for the basis functions in the sum. All of the discretized vector quantities utilized here will be of this form.

For geometries in reciprocal media (the only case considered here), the $\mathbf{Z}$ matrix is symmetric and complex-valued. As such, it may be decomposed into symmetric, purely real and purely imaginary components $\mathbf{R}$ and $\mathbf{X}$, respectively:

$$\mathbf{Z} = \mathbf{R} + j\mathbf{X} \tag{2.2}$$

Following Harrington and Mautz [3], one may consider a generalized eigenvalue problem:

$$\mathbf{Z}\vec{J}_n = \nu_n \mathbf{M}\vec{J}_n \tag{2.3}$$

where ν_n is the nth eigenvalue and $\mathbf{M}$ is an arbitrary weighting matrix. Harrington asserts that any symmetric $\mathbf{M}$ diagonalizes $\mathbf{Z}$, and with the choice

of $\mathbf{M} = \mathbf{R}$, one also obtains orthogonal radiated far fields. Letting $\nu_n = 1 + j\lambda_n$, these substitutions yield

$$(\mathbf{R} + j\mathbf{X})\vec{J}_n = (1 + j\lambda_n)\mathbf{R}\vec{J}_n \tag{2.4}$$

which may be simplified to the foundational eigenvalue problem of TCM:

$$\mathbf{X}\vec{J}_n = \lambda_n \mathbf{R}\vec{J}_n \tag{2.5}$$

For each eigenvalue λ_n with mode index n, there is associated an eigenvector surface current density $\vec{J}_n$ known as a characteristic (current) mode. Because $\mathbf{R}$ and $\mathbf{X}$ are real and symmetric, these eigenvalues and eigenvectors will be purely real. (Note that in the frequency domain, purely real currents (or currents with any constant argument) over the structure's surface merely indicate that the current is equiphase across the surface.) Furthermore, these modes are orthogonal with respect to radiated power and may be normalized to radiate unit power. Defining the symmetric product between two vectors $\vec{A}$ and $\vec{B}$ as

$$\left\langle \vec{A}, \vec{B} \right\rangle = \vec{A}^T \vec{B} \tag{2.6}$$

we obtain

$$\left\langle \vec{J}_m, \mathbf{R}\vec{J}_n \right\rangle = \left\langle \vec{J}_m^*, \mathbf{R}\vec{J}_n \right\rangle = \delta_{mn} \tag{2.7}$$

$$\left\langle \vec{J}_m, \mathbf{X}\vec{J}_n \right\rangle = \left\langle \vec{J}_m^*, \mathbf{X}\vec{J}_n \right\rangle = \lambda_n \delta_{mn} \tag{2.8}$$

$$\left\langle \vec{J}_m, \mathbf{Z}\vec{J}_n \right\rangle = \left\langle \vec{J}_m^*, \mathbf{Z}\vec{J}_n \right\rangle = (1 + j\lambda_n)\delta_{mn} \tag{2.9}$$

The middle term results from the fact that the modes are purely real, hence equal to their complex conjugate. If the modes are expressed as root-mean-square (RMS) values, then the middle terms of these normalizations indicate that the modes radiate unit power.

The original formulation of TCM with continuous operators naturally leads to an infinite number of CMs. When discretized using finite dimension matrices, however, one may only obtain at most N modes, where $\mathbf{Z}$ is an $N \times N$ matrix. Regardless, in practical usage of TCM, one typically only uses the most significant modes and truncates those of less significance. Measures of significance will be discussed shortly.

As mentioned earlier, in addition to current orthogonality, the far fields radiated by each CM are themselves orthogonal over the sphere at infinity. While this property won't be utilized here, it is of particular importance when using TCM for antenna pattern analysis and synthesis.

An important point to note here is that CMs, being eigensolutions, are derived without regard for excitation and hence are excitation-independent. Expressions will be given later for determining which and to what extent modes are excited for a given source.

2.1.2 Properties of CMs

As in many eigenvalue problems, the particular value of the eigenvalues λ_n in TCM convey useful physical information. Modes corresponding to $\lambda_n = 0$ are resonant modes, the most effective at radiating energy. Modes for which $\lambda_n > 0$ are inductive modes, storing more magnetic than electric reactive energy. Conversely, $\lambda_n < 0$ corresponds to capacitive modes, which store more electric than magnetic energy. As an eigenvalue may lie anywhere in the range $(-\infty, \infty)$, one convenient representation of this information is in the form of the characteristic angle, α_n:

$$\alpha_n = 180^\circ - \arctan(\lambda_n) \tag{2.10}$$

For most electrical engineers, this gives a more clear description of the nature of the modes:

$$90^\circ \leq \alpha_n < 180^\circ, \quad \text{Inductive Mode} \tag{2.11a}$$

$$\alpha_n = 180^\circ, \quad \text{Resonant Mode} \tag{2.11b}$$

$$180^\circ < \alpha_n \leq 270^\circ, \quad \text{Capacitive Mode} \tag{2.11c}$$

Physically, the characteristic angle represents the phase angle between the CM's surface current density and the electric field it radiates. As the modes' eigenvalues tend towards $\pm\infty$ ($\alpha_n = 90^\circ$ or $\alpha_n = 270^\circ$), they become more and more ineffective at radiating.

Alternatively, a mode's effectiveness at radiation (nearness to resonance) may be measured by its modal significance (a measure first mentioned by

Austin and Murray [9]), given by

$$\mathrm{MS} = \frac{1}{|1 + j\lambda_n|} = \frac{1}{\sqrt{1 + \lambda_n^2}} \tag{2.12}$$

The modal significance obviously lies in the range $0 \leq \mathrm{MS} \leq 1$, with $\mathrm{MS} = 1$ corresponding to resonance.

A particularly useful property of CMs is their use as basis functions for expanding the current excited on a structure by a given source. A surface current density $\vec{J}$ on such a PEC structure may be written as the infinite sum of appropriately weighted CMs, where n refers to the mode index:

$$\vec{J} = \sum_n c_n \vec{J}_n \tag{2.13}$$

For an incident tangential electric field $\vec{E}^i$ over the surface of the structure as the source, the modal weights c_n can be obtained using the orthogonal properties of the CMs. Plugging equation 2.13 into 2.1 and taking the symmetric product of both sides with $\vec{J}_m$ gives

$$\sum_n c_n \left\langle \vec{J}_m, \mathbf{Z}\vec{J}_n \right\rangle = \left\langle \vec{J}_m, \vec{E}^i \right\rangle \tag{2.14}$$

Using the orthogonality relation of equation 2.9 reduces the infinite sum to the single term where $m = n$. Solving for c_n yields

$$c_n = \frac{\left\langle \vec{J}_n, \vec{E}^i \right\rangle}{1 + j\lambda_n} = \frac{V_n^i}{1 + j\lambda_n} \tag{2.15}$$

The symmetric product in the numerator is known as the modal excitation coefficient, V_n^i, and is a measure of how strongly a given excitation couples to a given mode.

Remembering that TCM is really an operator theory (and that most of the equations presented here are the finite discretizations of that theory), an alternative definition for the modal excitation coefficient may be derived using reciprocity from classical electromagnetic theory. Recall the reciprocity theorem for two electric current sources a and b with currents $\vec{J}_a$ and $\vec{J}_b$ defined in a volume V_{src}, with radiated electric fields $\vec{E}_a$ and $\vec{E}_b$, respectively. If V_{src} contains only reciprocal media (even if inhomogeneous or anisotropic),

then

$$\iiint_{V_{src}} \vec{E}_a \cdot \vec{J}_b \, dV = \iiint_{V_{src}} \vec{E}_b \cdot \vec{J}_a \, dV \tag{2.16}$$

which states that the integral of the inner product of a's fields with b's current over the region where b is defined (has nonzero current) is equal to the opposite case, the integral of the inner product of b's fields with a's current over the region where a is defined. For the case of TCM, the CMs (consider these as source b) are only defined over the surface of their structure, S, so the triple integral reduces to a double surface integral. This integration will be equal to the integral (over the excitation source's current) of the modes' radiated fields times the current of the source:

$$\iint_{S} \vec{E}_{src} \cdot \vec{J}_n \, dS = \iiint_{V_{src}} \vec{E}_n \cdot \vec{J}_{src} \, dV \tag{2.17}$$

The left-hand side of this equation is nothing more than the usual modal excitation coefficient V_n^i, while the right-hand side offers an alternative definition for it as obtained using reciprocity. Switching back to the discretized form, we have

$$V_n^i = \left\langle \vec{J}_n, \vec{E}^i \right\rangle = \left\langle \vec{E}_n, \vec{J}^i \right\rangle \tag{2.18}$$

Both the usual (center) and reciprocal (right) definitions will be of use later.

Just as the CMs may be used as a modal expansion of an arbitrary current on a PEC structure, their radiated fields may be used to expand the radiated field of this arbitrary current. Specifically, if a CM $\vec{J}_n$ radiates an electric field $\vec{E}_n$, a current having the expansion given in equation 2.13 radiates the electric field $\vec{E}$, expandable as

$$\vec{E} = \sum_n c_n \vec{E}_n = \sum_n \frac{V_n^i \vec{E}_n}{1 + j\lambda_n} \tag{2.19}$$

2.1.3 CMs Over Frequency

The inherent reliance of TCM on the method of moments (for the $\mathbf{Z}$ matrix) means that a given solution to its generalized eigenvalue problem is only for a single frequency of operation. Often one needs to know the behavior of a structure or antenna over a band of frequencies. Consequently, a TCM

analysis must be run at discrete frequency points chosen over the band of interest, with spacing suitably chosen for the problem at hand.

Depending on the particular application, the subset of the calculated modes actually used at each frequency may be selected based solely on some measure of significance, or it may also utilize information about the modes at adjacent frequencies. It should be mentioned that this latter case, known as eigenvector "tracking", can allow one to view how eigenvalues or eigenvectors evolve over frequency. (Accurate tracking can be tricky since CMs are not constant with frequency; see Figure 2.3. A good approach usually involves computing vector correlations between solutions separated by small frequency steps, perhaps with more elaborate algorithms as in the work of Capek et al. [10].) Tracking shows, for example, that most modes start as capacitive, pass through resonance, and become inductive as the frequency is increased, although a few circulating current modes are inductive over the entire frequency band. This information can be useful when determining which modes, at which locations, and at what frequencies to excite a given antenna structure. Nevertheless, not all applications require this information or mode tracking. In this thesis, where CMs are simply used as a convenient set of whole-domain basis functions to expand a structure's current and more easily estimate input impedance, tracking actually isn't necessary and hence isn't used.

A brief, concrete example of the CMs of a basic structure will now be offered. The seven most significant modes at 1.0 GHz of a two-dimensional PEC plate are plotted in Figure 2.1; at this frequency, the plate's dimensions are roughly $\lambda/3$ by $\lambda/30$. For this example, these modes were then tracked over frequency. A plot of their characteristic angles from 1.0 GHz to 5.0 GHz is given in Figure 2.2. Modes 1, 4, and 7 resonate ($\alpha_n = 180°$) in this range, while modes 2 and 5 remain capacitive, likely to resonate at higher frequencies. The remaining two modes (3 and 6) are circulating current (inductive loop) modes that radiate poorly. Finally, Figure 2.3 tracks mode 1 over a wide frequency range, showing how a mode's pattern can dramatically change over frequency.

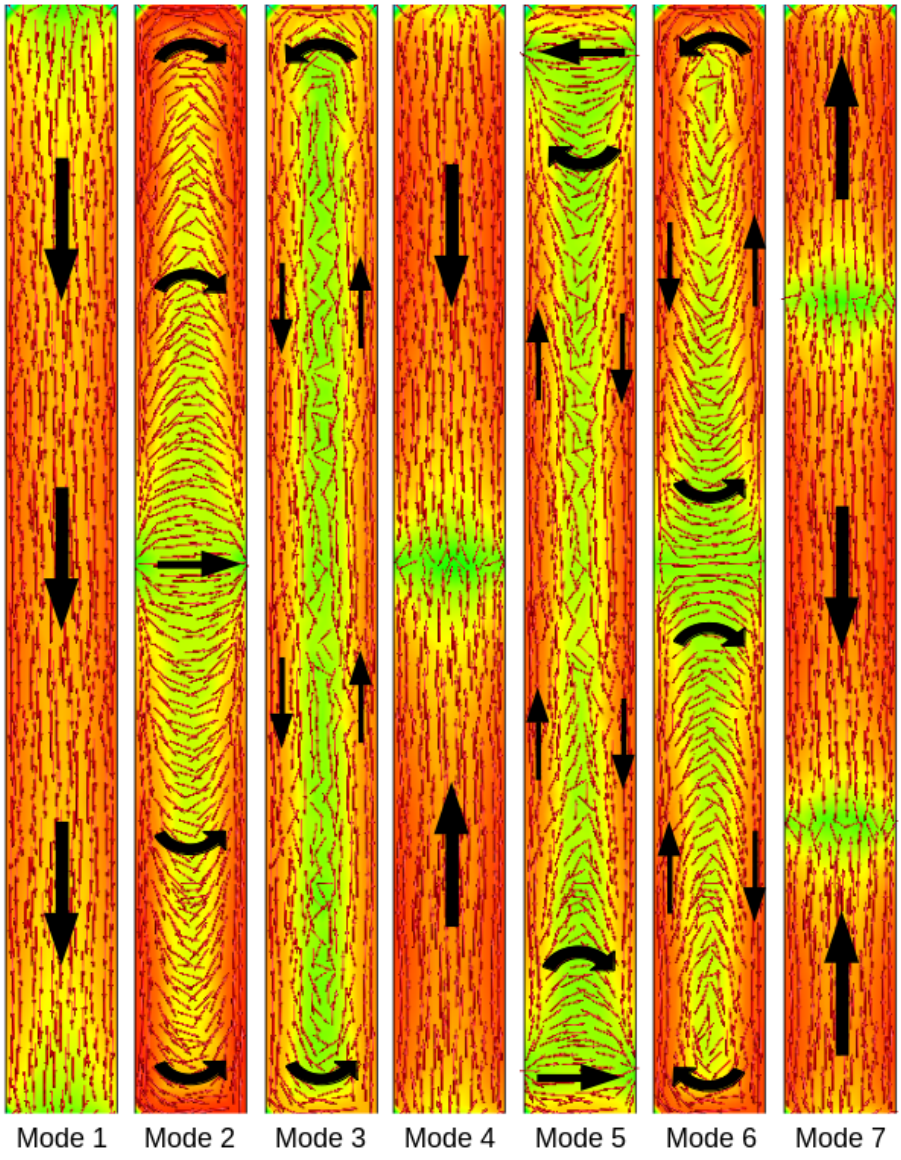

Figure 2.1: Plot of the first seven characteristic modes of a 100 mm by 10 mm PEC plate at 1 GHz. For ease of visualization, current magnitudes are color-coded on a decibel scale and black arrows showing general direction trends have been added.

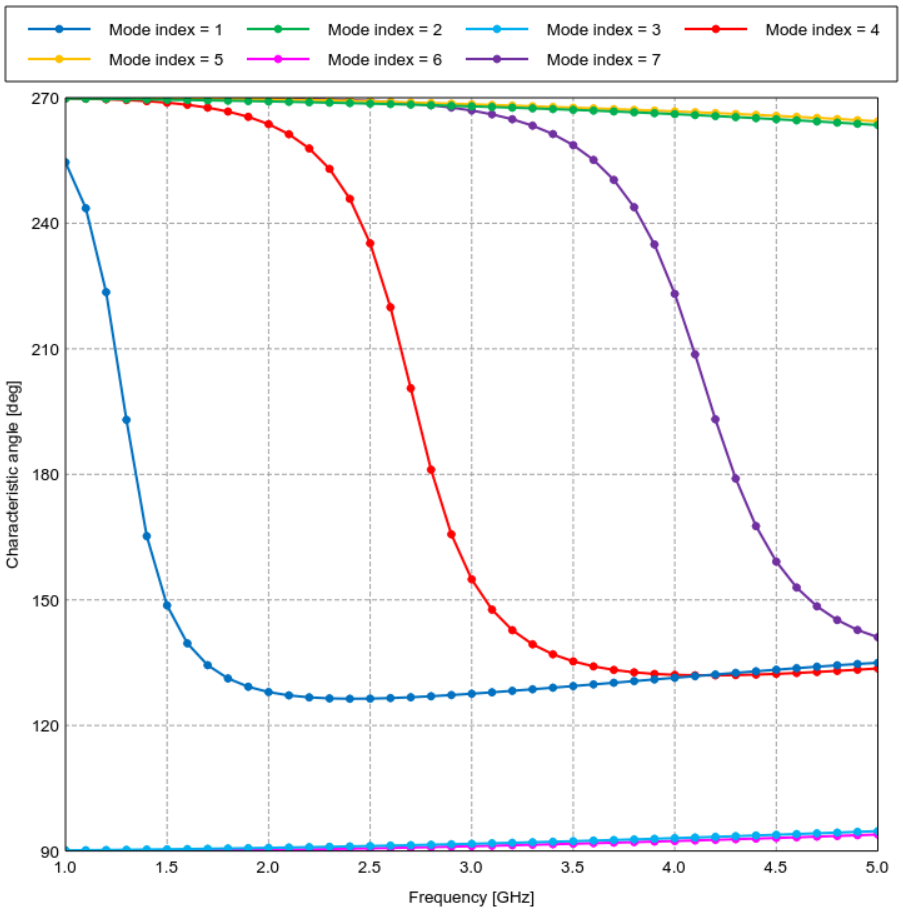

Figure 2.2: Plot of the characteristic angles over frequency for the modes of Figure 2.1.

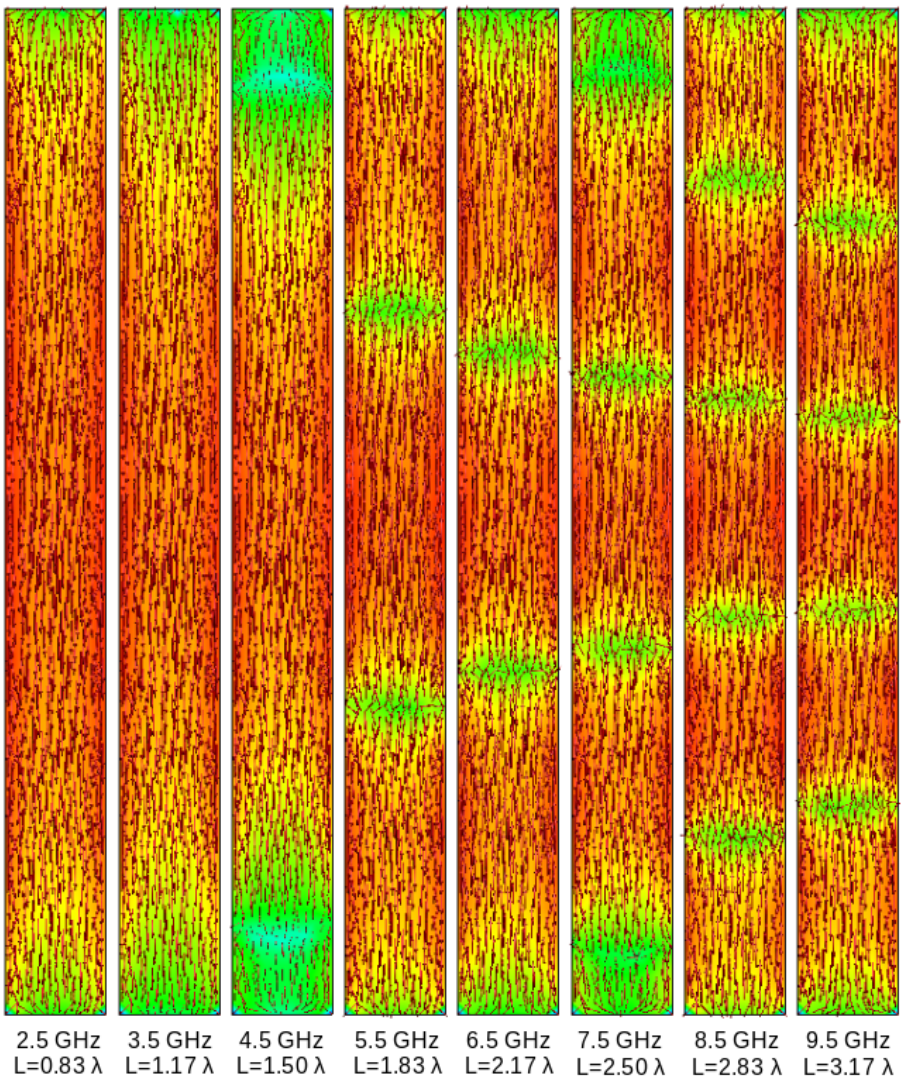

Figure 2.3: Variation with frequency of characteristic mode 1 (referenced at 1 GHz) for a 100 mm by 10 mm 2D PEC plate. L denotes the length of the plate in wavelengths at each frequency. Green and blue regions represent current nulls; current flows in opposite directions on either side of a null. Note that current magnitudes are color-coded on a decibel scale for ease of visualization.

2.2 Antenna Input Impedance in Literature

The topic of antenna input impedance is an important one and has been addressed in many different ways over the years. Since the focus of this thesis (explained in detail in Chapter 3) is on arbitrarily shaped microstrip patch antennas analyzed using TCM, only literature relevant to these topics will be discussed here.

As detailed in Carver and Mink's classic, comprehensive paper [11] on microstrip (patch) antennas (MSAs), work on these antennas was initially explored beginning in the 1950s, with research and development accelerating in the 1970s. Comprised of a metallic "patch" separated from a ground plane by a substrate (typically a thin, non-magnetic dielectric), MSAs are usually narrowband antennas operated at or near resonance. Consequently, their input impedance is sensitive to frequency, feed location, and antenna geometry (patch shape). To make MSA design feasible, a number of analytical approaches to estimating input impedance have been developed; chief among these are the transmission line model and the resonant cavity model. For rectangular patches with a feed placed along an axis of symmetry, the MSA may be modeled as a microstrip transmission line with the input impedance given by the radiation resistance (and reactive loading) suitably transformed by transmission lines of length equal to the feed probe's distances from the patch edges. Although a nice intuitive model, this approach isn't as accurate as other methods and only applies to particular feed points on rectangular patches, a potentially severe restriction. The other major analytical model according to Carver and Mink [11] is the resonant cavity model. Here, the space between the antenna's patch and ground plane is modeled as a lossy resonant cavity. By expanding the fields of this cavity in terms of TM_z modes, much more accurate estimates of input impedance (among other quantities) for arbitrary feed locations may be determined. While more generally applicable, this model nevertheless still suffers from restrictions to patches of certain canonical shapes (*e.g.* rectangles, circles, triangles).

A more recent development in MSA input impedance modeling is an eigenmode expansion by Shaker et al. in [12] and Shaker in [13]. In this approach, the modal expansion idea of the resonant cavity method is generalized to incorporate arbitrarily shaped patches, with the interior fields expanded in terms of the eigenmodes of the structure, as derived from the wave equa-

tion. With this method, Shaker is able to easily obtain accurate values of input resistance using only a small number of modes (on the order of 2 or 3). Good accuracy for input reactance is also claimed; however, this supposedly requires more modes and isn't addressed in any substantial detail. The extent of [13]'s treatment of input reactance of probe-fed patches is to model the probe as an additional inductance in series with the calculated input impedance. Shaker acknowledges that this simple model must be used with caution, as it is difficult and tedious to generalize to arbitrarily shaped patches and doesn't apply to off-axis feeding for rectangular patches (cases in which the feed probe's currents are asymmetric due to an asymmetric probe location). In short then, Shaker's eigenmode expansion method allows for accurate input *resistance* estimation for MSAs of arbitrary shape.

More accurate accounting for the input reactance of a microstrip antenna requires a more accurate model, not too surprisingly. One way to achieve this is explicitly include the feed probe in the antenna model and to model the coaxial cable's excitation as a combination of an electric current source along the feed pin and a radial (TEM mode) electric field over the annular aperture in the ground plane at the base of the feed pin (the opening of the coaxial cable). By the equivalence principle, the radial electric field may be replaced by an equivalent azimuthal magnetic current and the annular aperture in the ground plane shorted, forming a perfect ground plane. This is the approach taken by Chang-Hsiu and Hsu [14] and one approach taken by Chew et al. [15]. Chang-Hsiu and Hsu conclude that good results for the input impedance may be obtained when neglecting the aperture field when the aperture's size is small relative to the MSA's patch size. One of Chew et al.'s conclusions is that capacitance from the annular aperture has a more pronounced effect on the input impedance as the substrate thickness increases. This suggests that for thin substrates, one may obtain reasonable input impedances solely by modeling the feed as an electric current source along the feed pin, even when neglecting the aperture fields.

Turning to the topic of TCM, the input impedance of antennas using TCM was first addressed by Yee and Garbacz [16] in 1973. In this paper, the input admittance (and mutual admittance, for multi-port antennas) for an antenna or scatterer comprised of thin wires is derived for small delta-gap feeds using the structure's CMs as basis functions to expand induced current. Although Yee and Garbacz only consider thin-wire structures, likely for computational

feasibility reasons, this theory may also be applied to arbitrary structures in which the feed is located on a thin wire segment. (Indeed, this is the basis for the wire probe model developed later in Section 3.2.) A recent generalization of this approach is given by Ethier and McNamara [17], where the concept is extended to antennas representable with PEC surface meshes and driven by a delta-gap source in the surface mesh. As Ethier and McNamara are more interested in shape synthesis and the antenna's Q-factor, independent of feed location, the input impedance is only addressed theoretically and its accuracy not assessed.

A number of other papers apply TCM to the antenna feed problem, but none really focus on the accuracy of the modeled input impedance. Obeidat et al. [18], for instance, use TCM to explain the nature of series and parallel resonances in terms of CMs. An edge-fed, air-substrate MSA is one of three antennas analyzed, but the accuracy of its input impedance isn't addressed, nor are the results experimentally verified. Cabedo-Fabres et al. provide two preliminary uses of TCM for the analysis of air-substrate MSAs in [19] and [20]. In [19], the MSA is modeled as a metal patch in air over a ground plane, with TCM merely used to analyze the CMs' patterns on the patch. The MSA with an actual coaxial feed probe is then modeled using a conventional electromagnetic solver, and the resulting total induced current on the patch qualitatively compared to the previously computed CMs. In [20], TCM is used to analyze (among other things) a triangular MSA for purposes of radiating with circular polarization. Two of the patch's modes are selected as having desirable shapes (both nearly linear and orthogonal in space), and a suitable feed location found at a frequency and location on the structure where the modes' currents are equal in magnitude and are in phase quadrature (determined from the characteristic angles). In both papers, matters of input impedance or of feed modeling with TCM are not considered; the feed is merely viewed as a small excitation to be added at the end of the design process, with location chosen for strong coupling to the desired mode(s).

Two papers do specifically focus on input impedance modeling with help from TCM. In [21], Adams and Bernhard examine the modes of a dipole antenna over frequency and use these to derive broadband equivalent circuit models for the input impedance. Comparing the results to a full-wave simulation, very good agreement for both input admittance *and* susceptance is obtained over a $10:1$ bandwidth. Although application to more complicated

antennas (such as MSAs) is briefly addressed, such work remains to be done. In [22], Adams uses this approach to approximate input impedance by examining the CMs' radiated far-fields and determining the best fit to spherical harmonic fields; the input impedance is then modeled as a combination of the spherical harmonics' equivalent circuit models. The approaches of both [21] and [22] give good, wideband input impedance estimates, but are presently limited to simple antennas with a fixed, pre-placed feed. Overall then, application of TCM to modeling antenna input impedance in a manner suitable for determining a good feed location is currently an unexplored topic in the literature.

CHAPTER 3

APPROXIMATING ANTENNA INPUT IMPEDANCE WITH TCM

The benefits of input impedance approximation methods lie in their ability to assist the antenna designer in determining where to feed an arbitrarily shaped antenna. While any input impedance can theoretically be transformed to any required value by an appropriate matching network, such networks in practice can be lossy, bulky, and/or costly. The ability to obtain a more favorable input impedance simply by determining a suitable feed location is convenient and desirable. One way to achieve this is by utilizing impedance maps: surface plots of input resistance and reactance versus feed location. (See, for example, Shaker et al.'s work [12].) While impedance maps can be generated by an accurate simulation of the complete antenna for a large number of feed positions, such simulations are time-consuming. A better approach involves creating a model of the antenna sufficiently detailed enough to estimate its input impedance, but sufficiently simplified enough to facilitate the creation of impedance maps.

One way to do this is to model an antenna without a feed and obtain a set of complete, whole-domain basis functions for its currents; TCM offers one such possible set. The interaction of a feed with the antenna structure may then be more easily computed in terms of interactions with the basis functions. The virtual probe model developed in Section 3.1 takes this approach. As will be more apparent later, this turns out to over-simplify the antenna's geometry for the sake of speed and simplicity at the expense of input impedance accuracy (particularly input reactance). Trading off the speed of analysis for improved accuracy, the wire probe model of Section 3.2 approximates a microstrip patch antenna's coaxial feed probe by explicitly including a thin wire in its model to better account for the probe's effects. While this does slow down the analysis, the accuracy obtained is markedly better.

The two methods developed in this chapter serve to provide an estimate

of the input impedance for air-substrate, coaxial probe-fed, microstrip patch antennas over perfect ground planes. This highly specific class of antennas is the result of two constraints: the theory used and the ease of experimental fabrication and measurement. The restriction to air substrates is a consequence of using the basic TCM, which is only valid for PEC structures in free space. Although a generalized TCM exists, it is considerably more complicated and presently not as well researched or understood. The restriction to coaxial probe-fed microstrip patch antennas is due to the relative ease with which these antennas may be fabricated and measured (*e.g.*, no balun is required for connecting to conventional SMA coaxial cables). Probe-fed antennas are also of particular interest as nearly all TCM literature to-date dealing with antenna feeds is restricted to the delta-gap feed model. The requirement for a perfect ground plane, or at least a large, highly-conductive one in the real world, is because small or imperfect ground planes can significantly alter an antenna's performance and a study of these effects is not a part of this thesis.

3.1 Virtual Probe Model

One of the simplest manners in which to model the coaxial feed probe of a MSA is with an idealized electric current line source, since the antenna's coaxial feed (between the patch and ground plane) is a short, thin, current-carrying wire. This approach was used during early development of computer codes to analyze MSAs using the method of moments; see, for example, Pozar [23]. Here also, this model ignores the feed probe's thickness, the annular aperture in the ground plane, and, more significantly, radiation from the feed probe. It should thus be more accurate the shorter the feed probe is. A further simplification is to assume that the source current on the feed probe (the line source) is uniform: no magnitude or phase variation will be introduced.

In a nutshell, the virtual probe model creates an electric current line source where the feed is to be located. The current induced on the MSA patch from this source is calculated, then the electric field radiated by the induced current is calculated. By integrating the field over the length of the line source, a voltage is obtained. Simple application of Ohm's law yields an

estimate of the input impedance. A more detailed explanation follows:

1. The antenna is first modeled as a PEC patch in free space above an infinite ground plane. The patch is suitably meshed (discretized) and the **Z** matrix for the patch structure is computed. Note that the geometry mesh for TCM problems generally must be more dense than for standard method of moment solutions. For a more detailed analysis, see the paper by Eichler et al. [24].

2. Per the generalized eigenvalue problem defined in equation 2.5, the eigenvectors (characteristic current modes) and their eigenvalues are calculated for **Z** and are normalized to radiate unit power. The N most significant modes (eigenvalues nearest to zero) are then chosen per the desired significance cutoff criterion.

3. A uniform electric line source carrying current I_{src} is "placed" at the feed probe location, having a length t equal to the substrate height (distance between the patch and the ground plane).

4. Using the radiated modal electric fields $\vec{E}_n$ (unweighted, hence still normalized to radiate unit power), the modal excitation coefficients V_n^i for the first N modes are calculated with the reciprocal form given on the far-right of equation 2.18. The modal weighting coefficients c_n are then computed with equation 2.15. In compact form,

$$c_n = \frac{\left\langle \vec{E}_n, \vec{J}^i \right\rangle}{1 + j\lambda_n} \tag{3.1}$$

5. Knowing the degree to which each mode is excited, the actual radiated electric field may be obtained by the weighted sum of equation 2.19. Integrating this along the length t of the line current gives the induced voltage:

$$V_{ind} = -\int_0^t \vec{E} \cdot \vec{dl} = -\sum_n c_n \int_0^t \vec{E}_n \cdot \vec{dl} \tag{3.2}$$

6. Finally, the estimate for the input impedance is given using Ohm's law:

$$Z_{in} = \frac{V_{ind}}{I_{src}} \tag{3.3}$$

3.2 Wire Probe Model

One of the limitations of the virtual probe model is that the CMs are calculated for the antenna structure without a feed. The assumption implicit in this, of course, is that the actual feed doesn't significantly perturb the CMs of the antenna. A better approach is to explicitly model the feed in simplified form. To do this, the wire probe model approximates the coaxial feed as a thin wire between the MSA's patch and ground plane. A uniform electric field is excited along the length of the wire and the input impedance again estimated from the integral of the electric field along the wire divided by the induced current in the wire.

A more thorough outline of this method is as follows:

1. The antenna is first modeled as a PEC patch in free space above an infinite ground plane. At the location of the coaxial feed pin, a thin wire is placed which connects the ground plane to the patch. Here, "thin" merely indicates that only longitudinally directed currents may flow on the wire. After the wire is placed, the patch is meshed as is appropriate for the frequency of interest and the $\mathbf{Z}$ matrix computed (again, keeping in mind that TCM calculations usually require denser meshes than standard method of moments calculations).

2. Next, the CMs and their eigenvalues are calculated for the MSA based on the TCM eigenvalue equation, equation 2.5, then the CMs are normalized to radiate unit power and the N most significant modes taken.

3. For the given structure mesh, the element(s) corresponding to the wire feed are determined. A uniform (constant magnitude and phase) electric field $\vec{E}^i$ is assumed along the length of the wire, and per equation 2.18 and equation 2.15, the first N modal excitation coefficients V_n^i and modal weightings c_n are computed. Compactly,

$$c_n = \frac{\left\langle \vec{J}_n, \vec{E}^i \right\rangle}{1 + j\lambda_n} \tag{3.4}$$

4. With the modal weightings, the current on the patch and feed wire can be obtained from the modal sum of equation 2.13. Taking the incident (source) electric field and integrating over the length of the feed wire

gives the impressed source voltage

$$V_{src} = -\int_0^t \vec{E}^i \cdot \vec{dl} \tag{3.5}$$

Taking the induced current at the base of the feed wire I_{ind}, an input impedance may be calculated as

$$Z_{in} = \frac{V_{src}}{I_{ind}} \tag{3.6}$$

3.3 Impedance Maps

One of the benefits of an accurate and affordable method for estimating antenna input impedance is that it enables the generation of impedance maps. Such maps plot input resistance or reactance over the surface of an antenna as a function of feed position. (Alternatively, the magnitude and phase angle of the input impedance may also be plotted.) In other words, for a given position, they show what the input impedance would be if the antenna were fed at that point. Impedance maps are particularly useful to the engineer who already has a designed antenna, but wishes to know where the best (or a better) feed location would be. Recent and prominent usage of impedance maps can be found in Shaker et al.'s work in [12] and Shaker's work in [13].

At their fundamental level, impedance maps may be used to match an antenna to a desired impedance simply by taking the locus of points with the desired input resistance and locating its intersection with the locus of points having the desired input reactance. (Again, a similar procedure exists for impedance magnitude and phase maps.) As such an intersection may not exist for a given antenna, impedance maps may also be used to determine the "best" input impedance obtainable, *e.g.* obtainable input resistances for zero input reactance, or input impedances closest in magnitude to $50\,\Omega$. From a practical fabrication standpoint, impedance maps also provide a measure of input impedance sensitivity. Regions on a map where impedances change rapidly indicate locations where small fabrication errors could significantly alter the input impedance. For maps generated from TCM-based approaches, modal properties may also be displayed. If strong excitation of a given CM is desired, say because it has a high modal significance, the fraction of input

energy that couples to that mode (the fraction of the input impedance attributable to that mode) can also be plotted as a function of position, showing feeding locations that excite the mode. Examples of impedance maps will be provided in Section 4.4.5 for the particular case study of Chapter 4.

CHAPTER 4

CASE STUDY: AN L-SHAPED MSA

In order to validate the derived input impedance estimation methods, an L-shaped microstrip patch antenna was designed, fabricated, experimentally measured, and compared with various simulations. The details of this particular case study are given in this chapter.

4.1 Design and Fabrication

Based on the developed theory, any air-substrate, coax-fed MSA would suffice for a real-world examination. I decided that the patch should have a non-canonical shape to emphasize the general applicability of the two TCM-based theories, yet should still be relatively easy to construct. Furthermore, I wanted to examine the patch for different fractions of a wavelength in size. With these requirements in mind, I settled on a symmetric L-shape with dimensions including a quarter- and half-wavelength in the frequency range of measurement. By picking these to occur at 3.0 GHz and 6.0 GHz, respectively, the patch's primary dimensions were set at 25.0 mm on a side, as depicted in Figure 4.1. The reason for these frequencies was a compromise between fabrication ease and measurement ease. Much lower in frequency would complicate antenna pattern measurements, requiring a larger, bulkier standard gain horn and potentially encroaching on the near-field of the antenna; much higher in frequency would make most of the antenna's dimensions small enough to be difficult to accurately fabricate. (As it turns out, the far-field requirement is less critical for the work here, since pattern measurements remain as future work to investigate.) Actual measurements were taken over the range of 2.0 GHz to 7.0 GHz, enclosing the two primary design frequencies.

With the patch itself designed, the patch's height above the ground plane

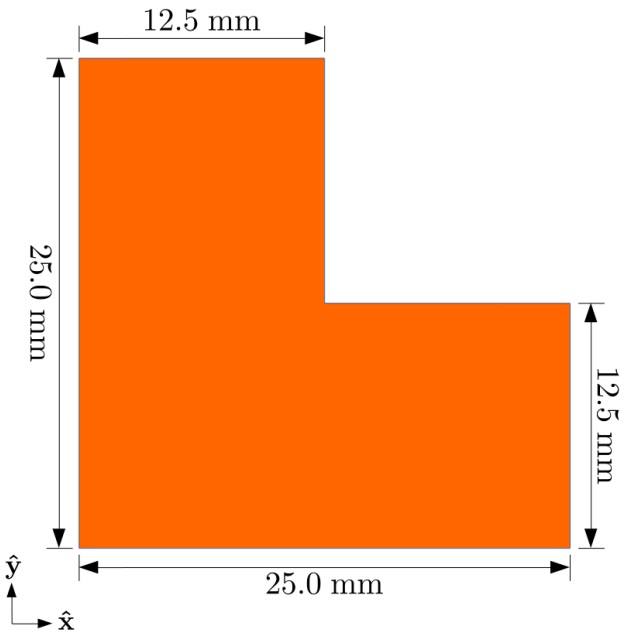

Figure 4.1: A top view of the L-shaped patch, showing dimensions. For the depicted coordinate system, the origin is located on the lower left corner of the patch.

needed to be determined next. For typical MSA design, choice of this parameter is important since it influences bandwidth, among other factors. Since I wasn't designing this antenna to meet any performance specifications, however, this parameter could be chosen fairly freely. Keeping the height small relative to the shortest wavelength of operation was one constraint: doing so should minimize feed probe radiation, which is undesirable for an MSA. Another influencing factor was structural soundness, since a key problem with air-substrate MSAs is the support of the patch. Although with a fixed probe position the patch could simply be supported by the feed pin, working with such a fragile design could quickly become tedious, especially given the need to relocate the probe to multiple positions. To add additional support, a block of structural foam (Rohacell ®) having a permittivity similar to air was tacked to one leg of the L with a dot of super glue. Since the exact value of the patch height wasn't critical, I chose it to be the same thickness as the available foam for convenience. Thus, the L-patch MSA was designed with a patch height of $t = 4.0\,\text{mm}$, corresponding to a bit less than $\lambda/10$ at 7.0 GHz, the highest frequency measured.

Fabrication of this antenna was done using 0.45 mm-thick copper for the

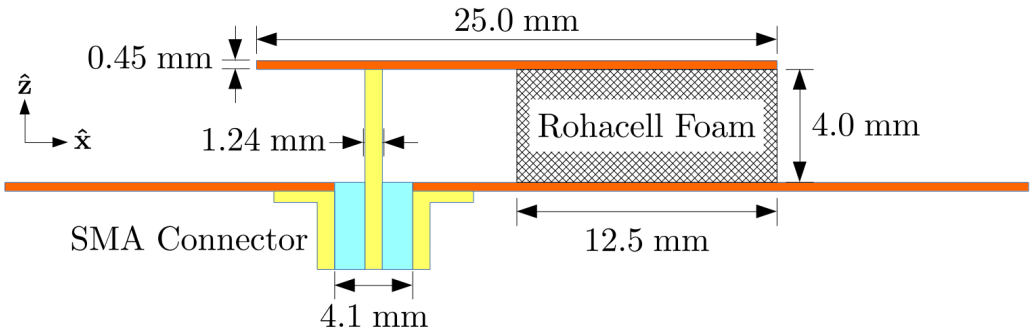

Figure 4.2: Dimensions (not to scale) of the fabricated patch and feed.

patch. A coaxial SMA connector was used for the feed probe, having an inner pin diameter of 1.24 mm and a Teflon dielectric of outer diameter 4.1 mm; see Figure 4.2 for a schematic and Figure 4.3 for a close-up picture of the patch and feed probe. The coax probe was mounted through a small square of copper (0.45 mm thick and about 120 mm on a side) serving as a local, structural ground plane. Since the theoretical design included an infinite ground plane, obviously physically impossible, the experimental antenna's full ground plane was realized using a large copper circle with a radius of 300 mm (2λ to 7λ over the measured frequency range). The L-patch antenna and its small, square ground plane were attached to this circle with conductive copper tape (see Figure 4.4). The relatively large dimensions of the ground plane were chosen so that its finite size would have negligible effect on the antenna's input impedance.

Such a large ground plane also enabled a convenient fabrication trick. Rather than move the feed probe itself to new positions, necessitating an arduous drilling of new holes, copper taping of old holes, and continual de-soldering and re-soldering of the coax connector, the patch itself was merely de-soldered, translated to a new position relative to the feed probe, then re-soldered to the probe. For a sufficiently large ground plane, shifting the patch's position slightly with respect to the plane's edges should have minimal effect, especially on the input impedance. For a given feed probe position, the patch was soldered in place and good (DC) electrical conductivity between the patch and the coax center conductor verified. For the first probe position, the patch was attached by placing a bit of solder on the coax feed pin, setting the patch on top, and attempting to heat the patch up enough (from above) that the solder would melt. The solder (silver spot) visible on

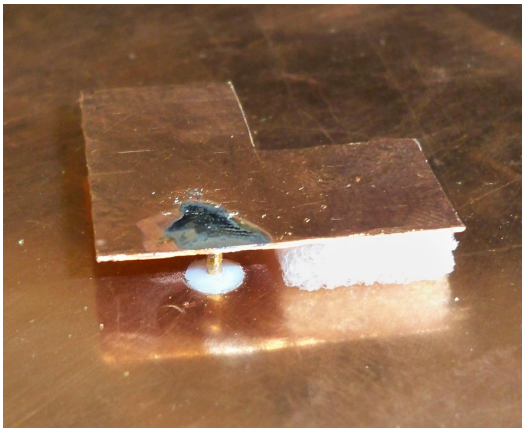

Figure 4.3: Close-up picture of the L-patch antenna. The solder (silver spot) on the top of the patch was an attempt to more efficiently transfer heat to the patch in order to solder it to the feed probe (gold pin below the patch). The white ring around the feed probe is the coaxial connector's Teflon dielectric. Visible on the right is the white structural foam.

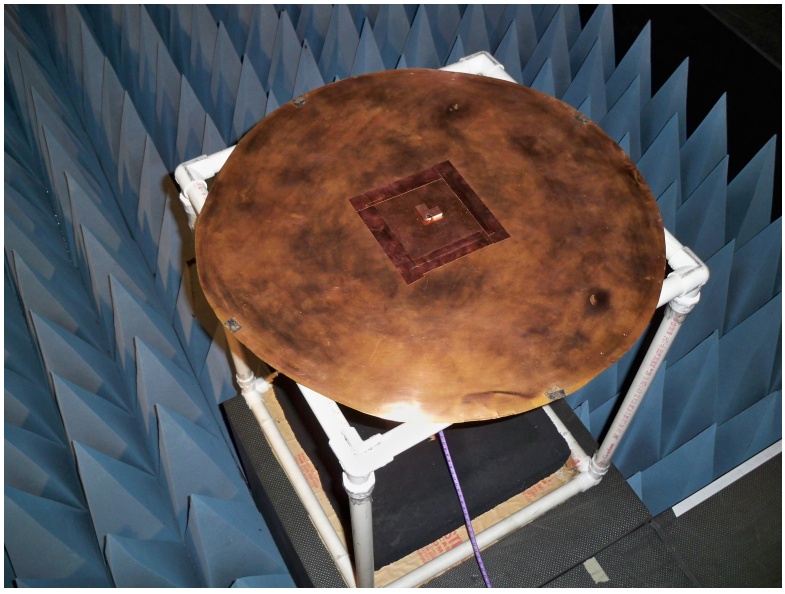

Figure 4.4: Picture of the L-patch antenna and its ground plane in the anechoic chamber. The conductive copper tape affixing the small square ground plane to the larger circular ground plane is clearly visible in the center.

the patch in Figure 4.3 was an attempt to more efficiently transfer heat to the patch for this purpose. In practice, this method proved to be slow, tedious, and not very effective. Ultimately, the best method found was to remove the coax feed pin by sliding it up (away from the ground plane), flipping the patch upside-down, and soldering the feed pin directly. The patch-pin structure could then be flipped right-side-up and slid back into place.

4.2 Measurement

A series of input impedance measurements were taken for the L-patch antenna for a variety of feed positions. For each probe position, the antenna was placed on a PVC pipe supporting structure inside the UIUC Electromagnetics Laboratory's anechoic chamber (see the picture in Figure 4.5). Scattering parameter (S_{11}) measurements were taken using an Agilent Performance Network Analyzer (model E8363C), swept from 2.0 GHz to 7.0 GHz with 1601 discrete frequency points. To ensure a good signal to noise ratio (especially given the somewhat lengthy cable required), the network analyzer's output power was increased to 0 dBm (1 mW). A total of 21 different feed probe positions were measured; these are plotted and tabulated in Figure 4.6. The feed pin's edge offset with respect to the origin (patch's lower left corner) was measured, then the probe center position calculated by adding the probe radius to these dimensions. (This is why all the positions end with a 2.) The first twenty positions, probes #0 through #19, were all measured during the same lab session, while #20 was added and measured about a month later.

Preliminary analysis showed that all of the S_{11} data for these positions had significant "curls" when plotted on a Smith chart, which led to small, superimposed ripples on the input impedance data. Due to the soldering technique used in which the feed pin was continually removed and re-inserted into the coax connector, there was concern that these ripples were indicators of an undesired air gap, possibly due to gradual wearing of the Teflon dielectric. Additional measurements of probe position #19 were taken both to investigate this matter and to check the measurement repeatability. The time-varying nature of the "curls" noticed this time around suggested that the issue was an artifact of the network analyzer. Increasing the frequency sweep time from a default 48 ms to a much longer but presumably safer

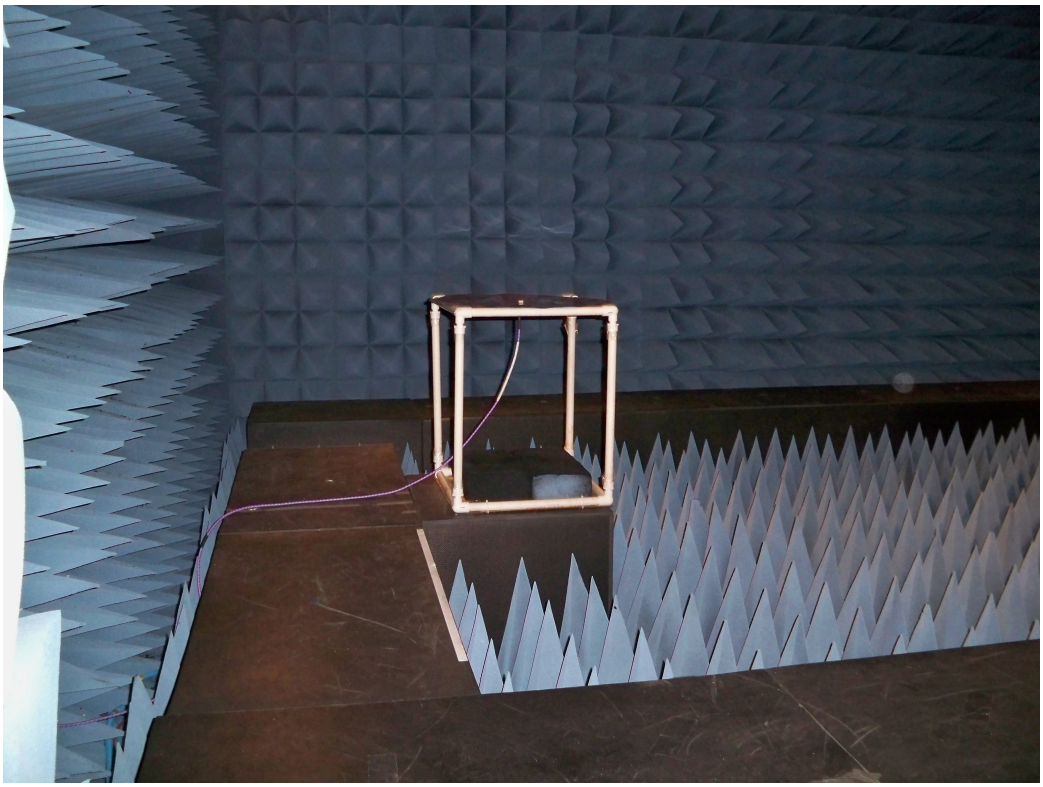

Figure 4.5: Picture of the L-patch antenna experimental setup. The antenna's ground plane was supported with a PVC pipe structure and placed at one end of an anechoic chamber.

500 ms resolved the issue by eliminating the "curls" altogether. Plots of the real and imaginary components of S_{11} are given in Figure 4.7, where line A was the first measurement, and lines B, C, and D were the follow-up measurements taken a month later. For lines B and C, the network analyzer's default 48 ms sweep time was used; after measurement B, the antenna was fully disconnected, the patch and feed pin structure removed from (slid out of) the coax connector, then reseated and remeasured. In this manner, everything just short of re-soldering the patch was done to check the experimental setup repeatability. Line D was yet another measurement iteration, but this time with the increased frequency sweep time. Finally, a 21st feed probe position (#20) was added near the end of the patch; this was also used to check repeatability, as well as to give data for an untested region of the patch. Excellent repeatability was obtained, as shown in Figure 4.8.

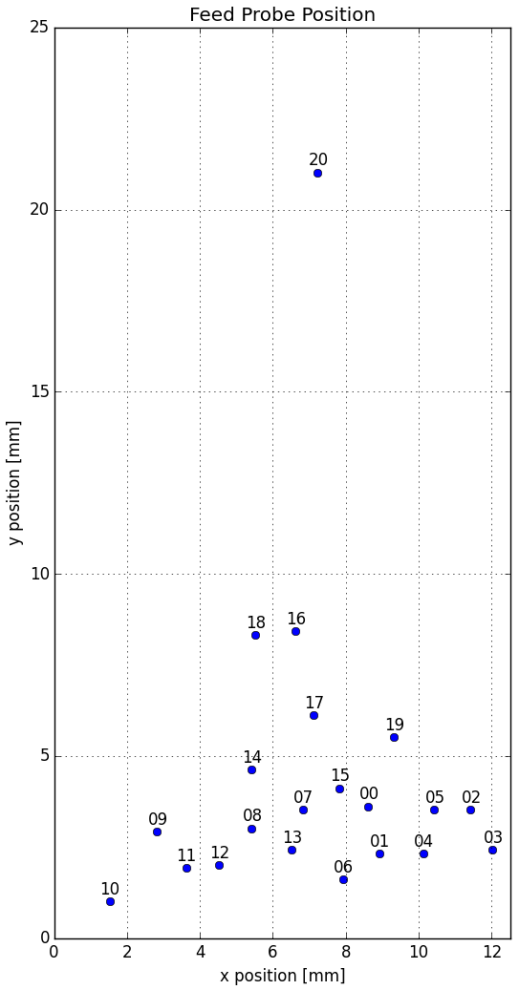

Probe Index	X [mm]	Y [mm]
0	8.62	3.62
1	8.92	2.32
2	11.42	3.52
3	12.02	2.42
4	10.12	2.32
5	10.42	3.52
6	7.92	1.62
7	6.82	3.52
8	5.42	3.02
9	2.82	2.92
10	1.52	1.02
11	3.62	1.92
12	4.52	2.02
13	6.52	2.42
14	5.42	4.62
15	7.82	4.12
16	6.62	8.42
17	7.12	6.12
18	5.52	8.32
19	9.32	5.52
20	7.22	21.02

Figure 4.6: Experimentally measured probe positions. The foam support corresponds to positions $x \geq 12.5\,\mathrm{mm}$.

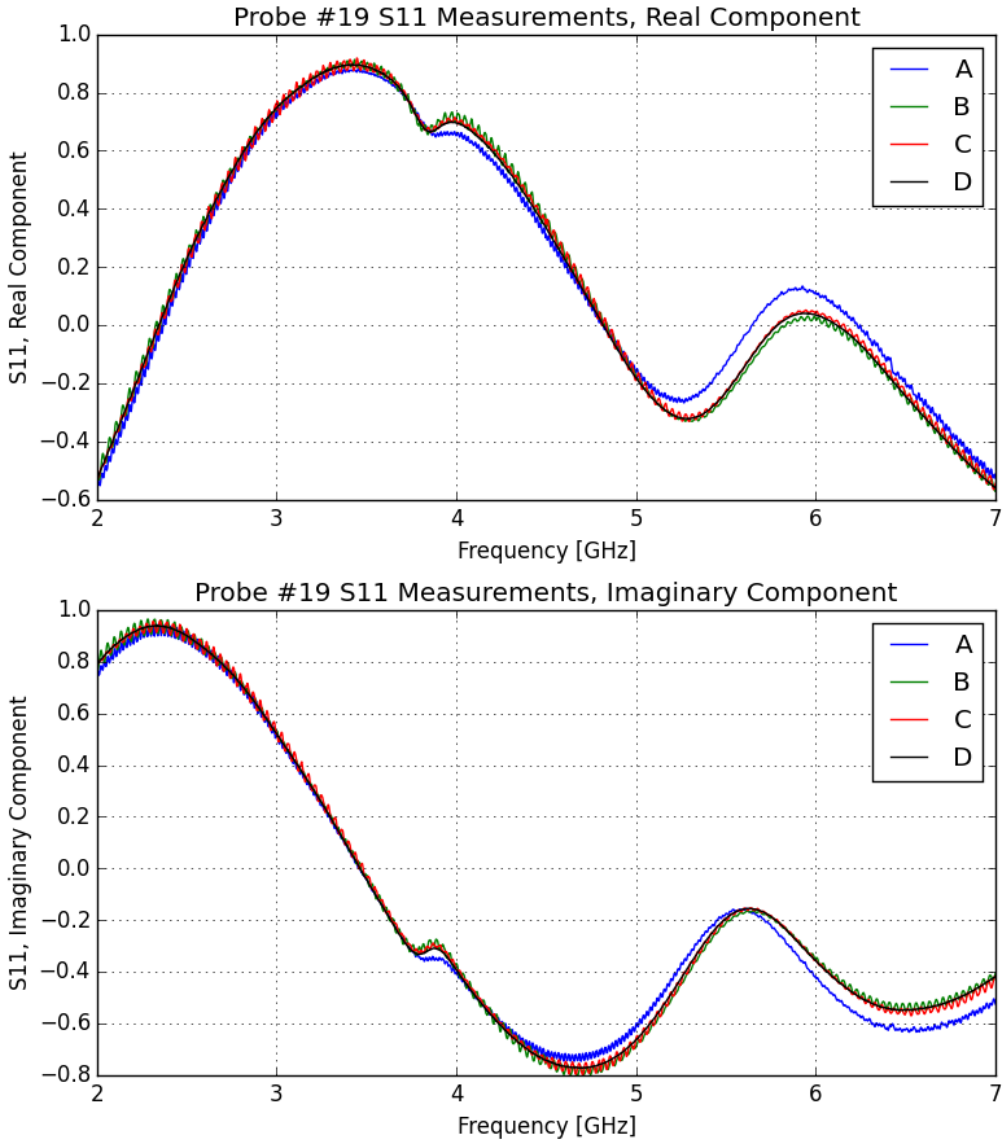

Figure 4.7: Measurement repeatability for probe position #19. Line A was the initial measurement, and lines B, C, and D were taken about a month later. Between B and C, the feed pin was removed from the coax connector and then reseated. Between C and D, the network analyzer's sweep time was increased from 48 ms to 500 ms, eliminating the ripples in the data.

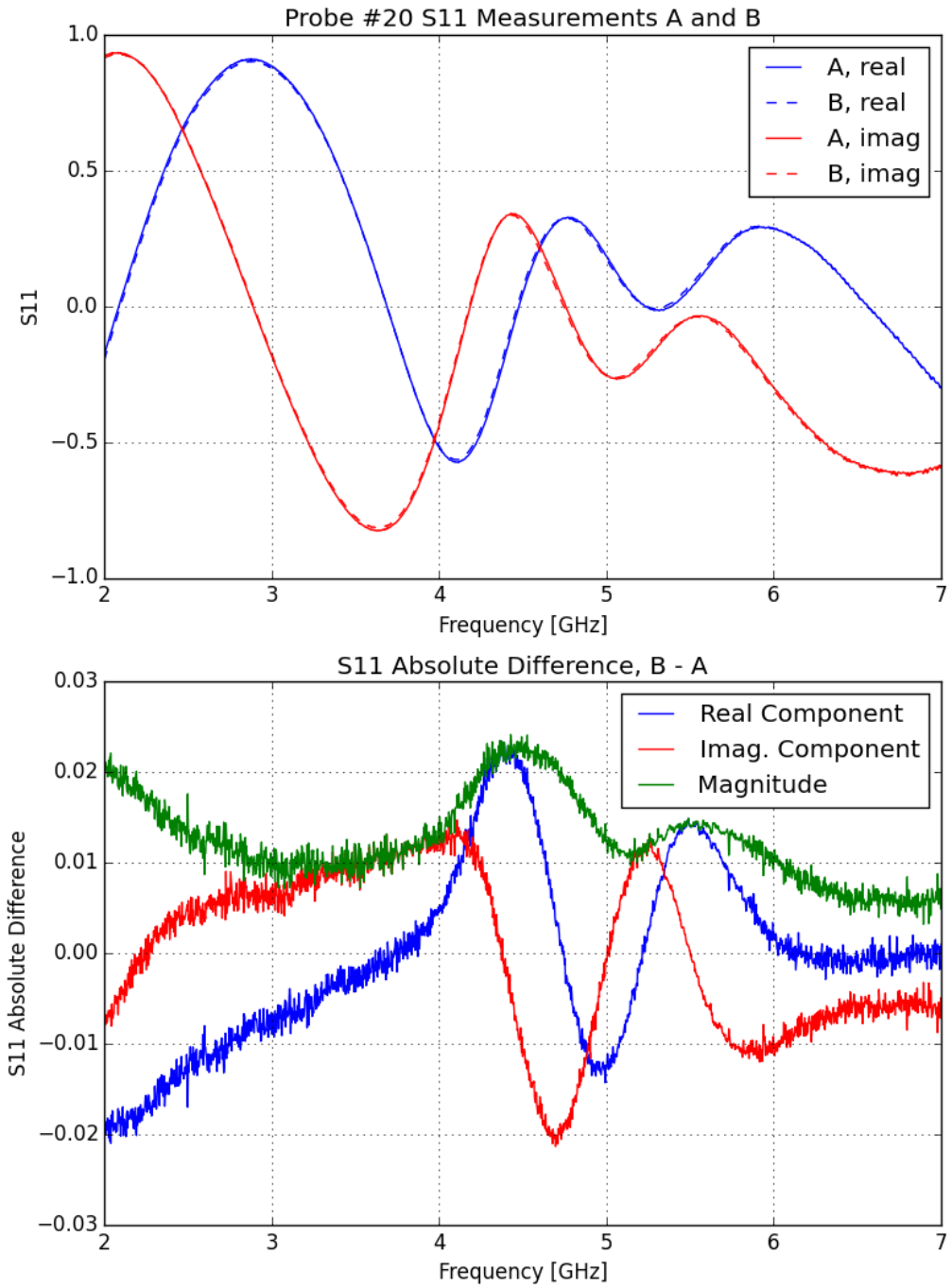

Figure 4.8: Comparison of two different S_{11} measurements of the antenna for the feed probe fixed in position #20. Very good repeatability is obtained, with the maximum magnitude difference between measurement A and B being less than 0.025. For these measurements, the network analyzer's frequency sweep time was set to 500 ms.

4.3 Simulations

Following experimental construction and measurement of the L-patch MSA, it was then analyzed using three different simulation methods: a commercial, full-wave finite element solver and the two TCM-based methods, the virtual and wire probe models.

4.3.1 HFSS™ Simulations

Analysis of the L-patch MSA with a standard finite element method full-wave solver was done for two reasons. First, by comparing these simulation results to experimentally measured results, a "sanity check" of sorts could be performed. Close agreement between the two data sets should indicate that the software model sufficiently captures the relevant details of the physical antenna. Conversely, close agreement should also indicate that the experiment is properly set up, is measuring the antenna with sufficient accuracy, and is free of major fabrication errors and unexpected disturbances (*e.g.*, verifying that the structural foam indeed minimally perturbs the antenna's performance). Second, analyzing the antenna with a full-wave solver (once the solver's results are experimentally verified) allows for more feed positions to be easily evaluated purely via simulation, cutting down on experimentation time.

With these reasons in mind, the L-patch MSA was modeled in the commercial solver ANSYS® HFSS™ (part of the ANSYS® Electromagnetics Suite, Release 15.0.7). Built above an infinite PEC ground plane, the patch itself was comprised of a thin copper plate having the same dimensions and substrate height as the experimentally measured antenna. For the antenna's coaxial SMA feed probe, a short segment of coaxial transmission line of length 2.05 mm was constructed below the ground plane and feeding up through it. Based on measurements of an actual SMA connector, the feed was designed with an outer conductor of radius of 2.05 mm, an inner conductor pin of radius 0.62 mm, and a Teflon® dielectric enclosed between the two. Although the outer conductor was modeled with PEC, the inner pin was modeled as copper and was extended up through the ground plane and connected to the patch as the antenna feed probe. The volume around the antenna and above the ground plane was set as free space, extending about 37.5 mm farther than

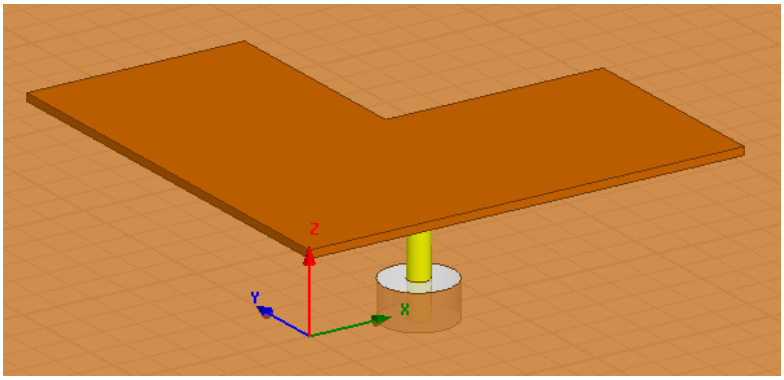

Figure 4.9: The L-patch antenna as modeled in HFSS. The L-shaped orange block is the copper patch, the gold post is the copper feed pin and coaxial cable's center conductor, the gray-white annular cylinder is the coaxial cable's Teflon dielectric, and the gridded, light orange background is the infinite PEC ground plane.

Table 4.1: HFSS-modeled material properties: relative permittivity (ϵ_r), relative permeability (μ_r), electrical conductivity (σ), and loss tangent (δ).

Material	ϵ_r	μ_r	σ [S/m]	δ
Copper	1	0.999991	5.8×10^7	–
Teflon	2.1	1	–	0.001

the antenna in all directions ($\lambda/4$ at 2.0 GHz). This volume was enclosed by a radiation boundary to allow this finitely truncated domain to mimic an infinite free space environment. A picture of the model in HFSS is shown in Figure 4.9; the free space volume and boundaries aren't pictured for clarity. The material properties used to model copper and Teflon are listed in Table 4.1.

In order to excite the antenna, a wave port was placed at the bottom of the coaxial feed cable, in effect connecting the short segment of modeled cable to an infinitely long waveguide of the same materials and cross-sectional dimensions. To ensure proper coupling of the cable to the antenna (per HFSS-recommended practices), a "perfect H boundary" was placed on the dielectric face in the plane of the ground plane (in other words, over the annular slot in the ground plane). Such a boundary in HFSS, when placed internally in the model, overrides the ground plane's PEC boundary condition and enforces continuity of the tangential magnetic field ($\vec{H}$) across the interface. This allows power to radiate through the annular slot in the ground plane [25].

With the excitation configured, the geometry was meshed (at the highest frequency, 7.0 GHz) and a driven modal solution calculated, converging for a maximum change in input S-parameter $\Delta S_{11} \leq 0.02$ and a maximum change in input port characteristic impedance of $\Delta Z_0 \leq 0.2$ %. Solutions for each of the 21 experimentally measured feed probe positions were then calculated at 41 frequency points from 2.0 GHz to 7.0 GHz via an interpolating sweep. An additional series of simulations were also run with the probe placed along a regular grid of positions for later impedance map generation.

4.3.2 Virtual Probe Model Simulations

Generation of the **Z** matrix for the virtual probe model was done using the commercial method of moments solver FEKO. An infinitely thin PEC plate with the MSA's patch dimensions was created and placed over a perfect, infinite ground plane. This model was then meshed with a maximum triangular element edge length of around 1.07 mm, corresponding to $\lambda/40$ at 7.0 GHz; the resulting mesh had 1116 elements and is pictured in Figure 4.10. The **Z** matrix was then calculated at 31 frequency points between 2.0 GHz to 7.0 GHz. Both this model and the wire probe model of Section 4.3.3 were initially simulated at 21 equally spaced frequency points, but 10 additional points were later added at frequencies where better resolution was needed due to the input impedance changing rapidly.

One of the attractive features of FEKO is the ease with which one can access and manipulate the files in which it stores its method of moments data. Documentation is provided explaining the file formats it uses to store **Z** matrices, current vectors, and near fields, just to name a few. Hence, even though FEKO is capable of computing CMs, this functionality wasn't used. Instead, calculation of the CMs of the structure at each solved frequency was done using custom Python[1] scripts to import the **Z** matrix, solve the generalized eigenvalue problem, normalize and sort the modes, and finally write the current modes (vectors) back into one of FEKO's files for easy visualization. This approach, documented in more detail in Appendix A, allows for easy development of new or non-standard methods, such as the virtual and wire probe models.

[1]Python is a powerful scripting language available for free at www.python.org.

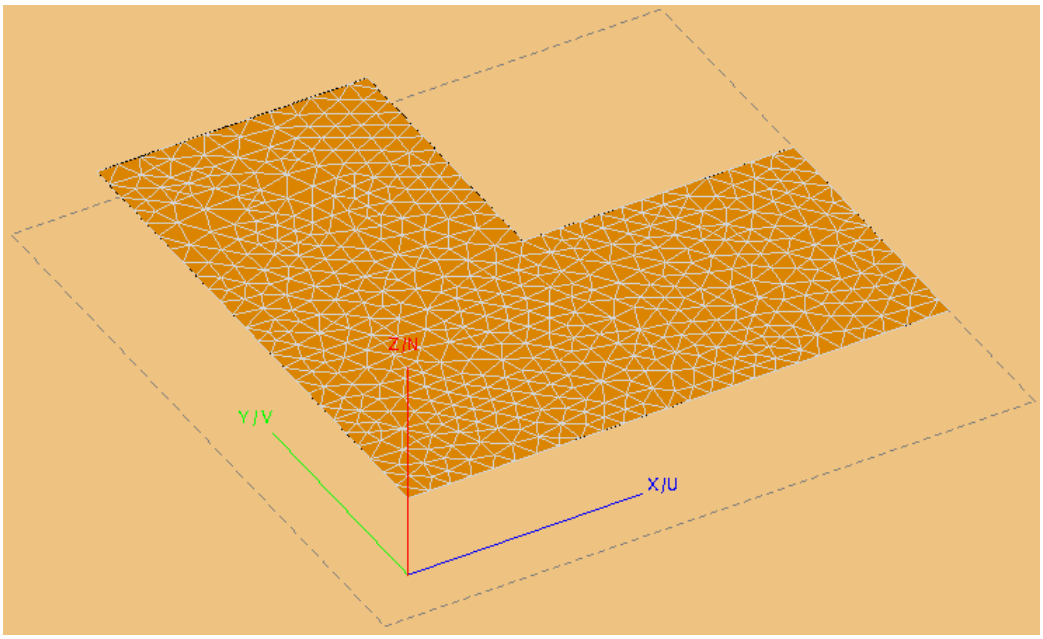

Figure 4.10: The FEKO model and mesh used for the virtual probe model.

Once the CMs of the antenna's patch have been determined, there are two ways of obtaining the modal excitation coefficients V_n^i for the virtual probe model. The first approach, using the center relation of equation 2.18, requires one to calculate the unit line current's (virtual probe's) radiated electric field's components that lie tangential to the patch surface. The modal excitation coefficient may then be computed using the CMs (the surface currents on the patch), $\vec{J}_n$, and this incident field, $\vec{E}^i$. Although a perfectly valid technique, this approach wasn't utilized because implementing it in a custom script outside of FEKO amounts to a somewhat involved process. One must import and work with the FEKO mesh of the patch, expand the CM current vectors on this mesh with the method of moments' basis functions, and compute the electric field radiated by the line current over the patch surface.

Alternatively, one may compute the modal excitation coefficients with the reciprocal form given on the right-hand side of equation 2.18. For this approach, one merely needs to know the CMs' radiated electric fields $\vec{E}_n$ at the virtual probe location. These can be easily computed using FEKO, thus leveraging its speed and accuracy. Another advantage is that the current vector $\vec{J}_i$ needed for this form requires no further computations: the excitation source is already a line current. This approach was the one used for the virtual probe model. Once the CMs had been calculated, their current

vectors were written back into FEKO's files. FEKO was then re-run with these surface currents, computing their radiated electric fields at a 3D grid of points between the patch and ground plane. By reading in this electric field data (again with custom Python scripts) and interpolating as necessary, the V_n^i's for the most significant modes were calculated and input impedances calculated per the method outlined in Section 3.1.

4.3.3 Wire Probe Model Simulations

A similar process was used for the TCM-based wire probe model, with generation of the **Z**-matrix again done in FEKO. As shown in Figure 4.11, the patch was constructed as a 2D PEC L-shaped plate above an infinite ground plane. A thin wire of radius $r = 0.62\,\text{mm}$ corresponding to the coax center feed pin was placed at the desired feed probe location, connecting the patch to the ground plane. Although wires in FEKO require specification of a radius, they only permit longitudinal (1D) current flow. Once constructed and with the feed suitably located, the FEKO model was meshed with a maximum triangular edge length of 2.0 mm (about $\lambda/20$ at 7.0 GHz) and with a wire segment length of 4.0 mm, allowing the feed to be constructed of a single wire, for simplicity. The resulting mesh has around 340 mesh triangles and a single wire. This structure wasn't meshed as densely as the one for the virtual probe model since near-field electric field values aren't needed for this method.

A total of 31 frequency points from 2.0 GHz to 7.0 GHz were simulated, same as with the virtual probe model simulations. For each probe position, the FEKO model was updated and meshed, the **Z** matrix generated and imported, and the CMs computed (using the method detailed in Appendix A). The modal excitation coefficients and resulting input impedances were calculated per the procedure in Section 3.2. As a brief note, care must be taken when integrating the source field (Equation 3.5) in discrete form (as with FEKO). For a uniform $\vec{E}^i$ of magnitude E^i, the discretized form of this integral is

$$V_{src} = E^i N_s \tag{4.1}$$

where N_s is the number of nodes over which the electric field is applied (the number of nonzero components in the discretized electric field vector of

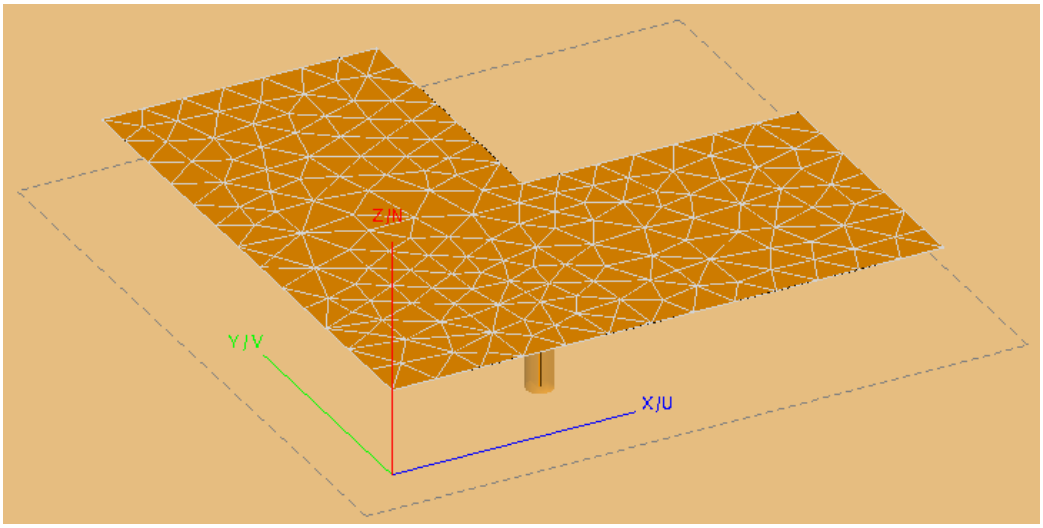

Figure 4.11: FEKO model and resulting mesh of the wire probe model of the antenna.

basis function coefficients). Accidental omission of the N_s factor is readily apparent as it manifests itself as an input impedance divided by this factor.

4.4 Results and Analysis

With the simulated data from HFSS and the two TCM-based methods, comparisons will be made to the experimental data and between the various methods. Overall, all three methods were able to provide good results, though the virtual and wire probe models showed a marked frequency shift and the virtual probe model's input reactance required additional compensation.

4.4.1 HFSS

One of the first steps taken was validation of the HFSS simulations against the experimental results. Although initial comparisons of HFSS's simulated input impedances differed drastically from the experimentally measured ones, comparison on a Smith chart quickly showed why. As shown in Figure 4.12, the two data sets differ merely by a frequency-dependent rotation. In other words, one set needs to be placed in series with a segment of transmission line, effectively moving the plane of reference for the measurement in a process known as de-embedding. Since HFSS's reference plane was already

established as lying along the antenna's ground plane, the experimental data were instead de-embedded. To accomplish this in a rigorous, repeatable manner, the HFSS S_{11} data were interpolated at the experimental data's 1601 frequency points, the experimental data de-embedded by a transmission line of length ℓ, and a least squares fit to find ℓ minimizing the absolute value of the difference in the two data sets performed. For interpolation, piecewise cubic Hermite interpolating polynomials were used (specifically, the `scipy.interpolate.pchip_interpolate` function from SciPy[2]); these had the benefit of smoothly and monotonically interpolating the data without the artificial oscillations or over-shooting sometimes present in other interpolation methods (such as with splines). For de-embedding, a lossless transmission line was taken with a characteristic impedance $Z_0 = 50\,\Omega$ and a phase constant $\beta = 2\pi/\lambda$ (that of free-space). For a length ℓ of such line, the transformed input reflection coefficient $\hat{S}_{11}$ is

$$\hat{S}_{11} = S_{11} e^{-2j\beta\ell} \tag{4.2}$$

After performing the least squares fit to all 21 of the experimental probe positions, the average value of $\ell = -12.3\,\text{mm}$ was taken and used to de-embed all of the experimental data for this and all subsequent comparisons. Although this value represents a length of transmission line, the negative quality simply corresponds to moving the measurement reference plane farther away from the network analyzer and closer to the antenna. Physically this value makes sense: for all of the measurements taken, calibration was performed with standards consisting of known loads attached to the end of the measurement cable. The exact plane of reference to which these standards calibrate the analyzer isn't precisely known, and the de-embedding necessary here suggests that this plane is somewhere inside the connector, not at its very endmost tip where the antenna's ground plane is. The de-embedding performed thus effectively moves the measurement reference plane out to the ground plane.

Overall, generally good agreement between the HFSS and (de-embedded) experimental data was obtained. Figures 4.12 and 4.15 compare S_{11} values on a Smith chart[3] for probe positions #0 and #12, while Figures 4.13 and 4.14

[2]SciPy is an open-source collection of Python modules (libraries) for scientific computing, and is available at www.scipy.org.

[3]Figure 4.15 and all subsequent Smith charts were generated using a custom modification of the `skrf.smith` routine in the open-source scikit-rf module [26].

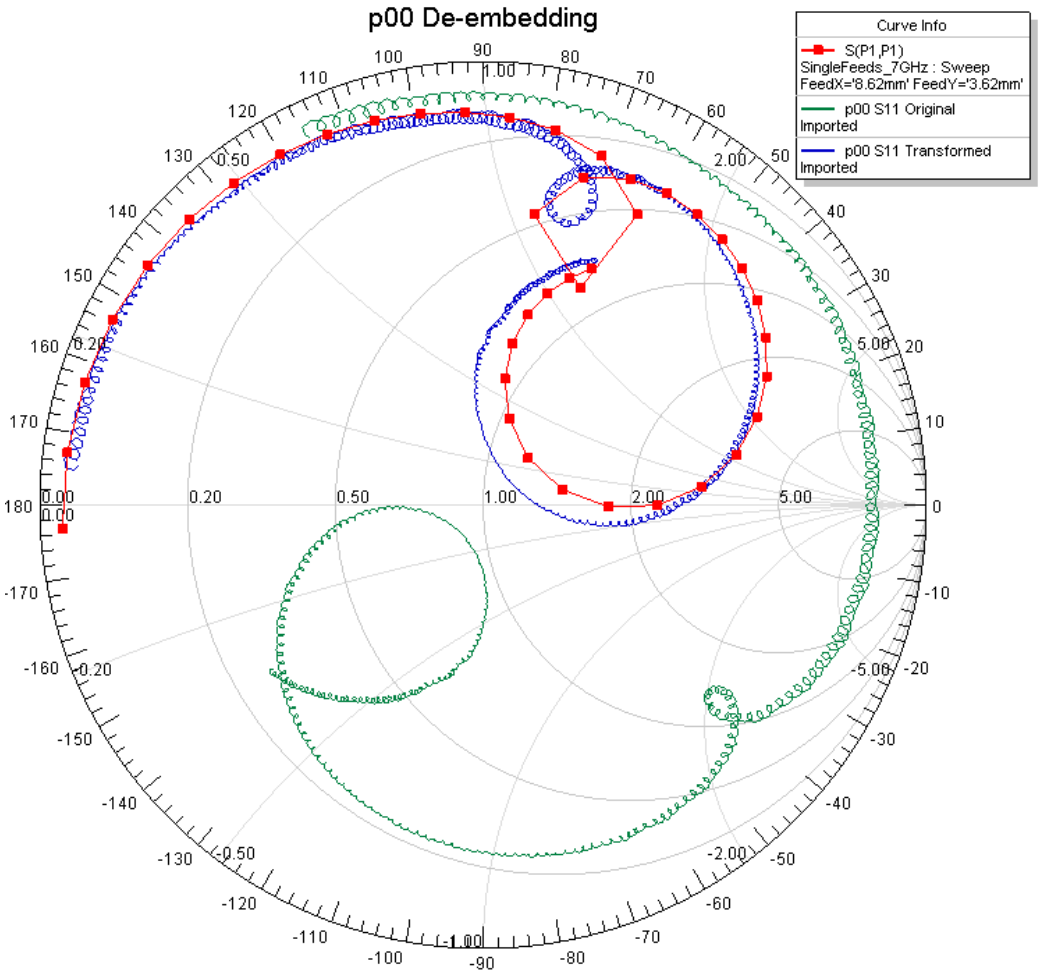

Figure 4.12: Plot performed in HFSS (normalized to 50 Ω) comparing reflection coefficients (S_{11}) at probe position #0 for the HFSS simulation (in red, with simulated frequency points denoted by square points), the raw experimental data (in green, labeled "Original"), and the transmission line de-embedded experimental data (in blue, labeled "Transformed"). The curls visible on the experimental data were finally eliminated for positions #19 and #20 by increasing the network analyzer's frequency sweep time.

compare input impedance values for these positions. For some of the probe locations, the HFSS data either indicates peaks a bit higher in frequency than they should be and/or differs slightly in input impedance values. Such differences may be attributed to the differences in the simulated model versus the real-world antenna. These potentially include:

- Ground plane loss, since the HFSS model used an infinite PEC ground plane
- Slight geometry differences, including the patch not being perfectly parallel to the ground plane, as well as the presence of structural foam and its affixing glue
- Slightly different material properties
- Loss in the feed probe's solder connection

Nevertheless, the results agree fairly favorably, as would be expected from a commercial solver. Unfortunately, although the data look quite similar, the slight frequency shift present in a number of the probe positions amounts to a fairly significant relative error when input impedances are compared. As a result, using HFSS to generate additional data for feed probe positions not experimentally measured (to which the TCM-based methods could be compared) isn't likely to be a good approach.

4.4.2 Virtual Probe Model

After the experimental data were properly de-embedded (with the help of HFSS), the accuracy of the TCM virtual probe model was analyzed. For the simulation setup described in Section 4.3.2, a total of 30 modes were computed. Inspection of the modes' patterns and total radiated power suggested that not all of these were valid. Most of the higher-order (larger eigenvalue) modes' current patterns were haphazard and unstructured, essentially looking like numerical noise. Although CMs' patterns aren't required to be neatly structured, all prior experience shows this to be the case in practice. The modes with "scrambled" current patterns were thus excluded. Additionally, a number of higher-order modes radiated considerably less than 1.0 W

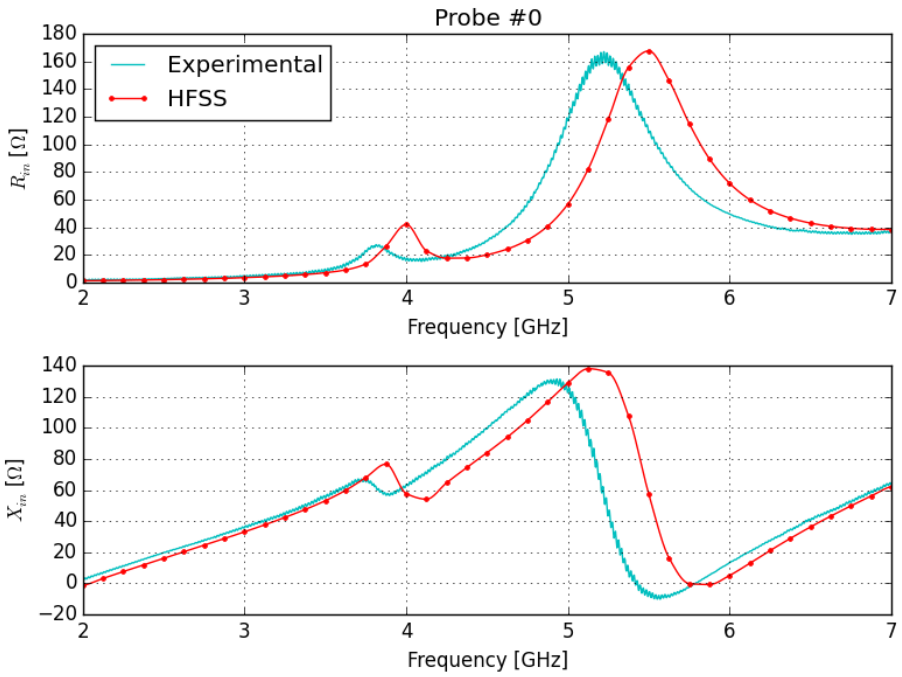

Figure 4.13: Probe position #0 input resistance and reactance for HFSS-simulated data versus experimental data. The points denote HFSS-simulated frequencies.

of power, despite being normalized to do so. (That is, they were normalized against the positive-semidefinite-coerced **R** matrix from Harrington and Mautz's method [4], as explained in Appendix A. FEKO's computation of their total radiated power used the original, indefinite version of **R**, hence the discrepancy.) These modes were deemed to likely be less accurate as well, and so were also excluded. In the end, the first 12 modes at each frequency with the smallest magnitude eigenvalues were kept. The ones at 2.0 GHz are shown in Figure 4.16, with one of the discarded "scrambled" modes shown in Figure 4.17.

The modes deemed valid were next returned to FEKO to compute the electric field near-field values, as needed for the virtual probe model. These field values were sampled on a regular grid, as detailed in Table 4.2, and the values needed for a given probe calculation linearly interpolated from these. Comparing the calculated input impedances with the (de-embedded) experimental data showed two issues. First, the raw data for the input resistance differed significantly, although closer inspection revealed that it was scaled up in frequency on the order of 8 %. Given that this TCM model is

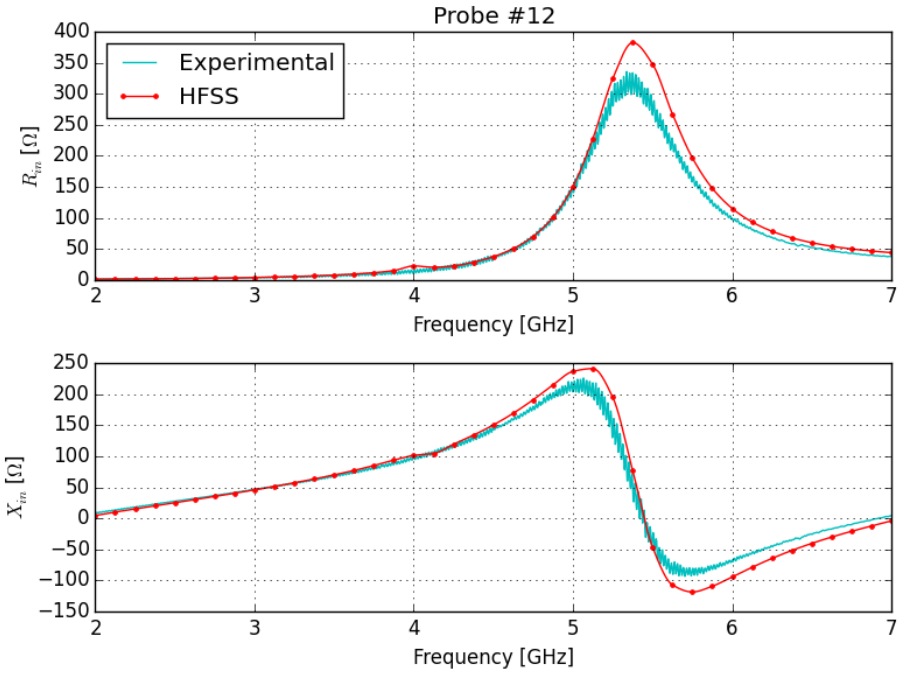

Figure 4.14: Probe position #12 input resistance and reactance for HFSS-simulated data versus experimental data. The points denote HFSS-simulated frequencies.

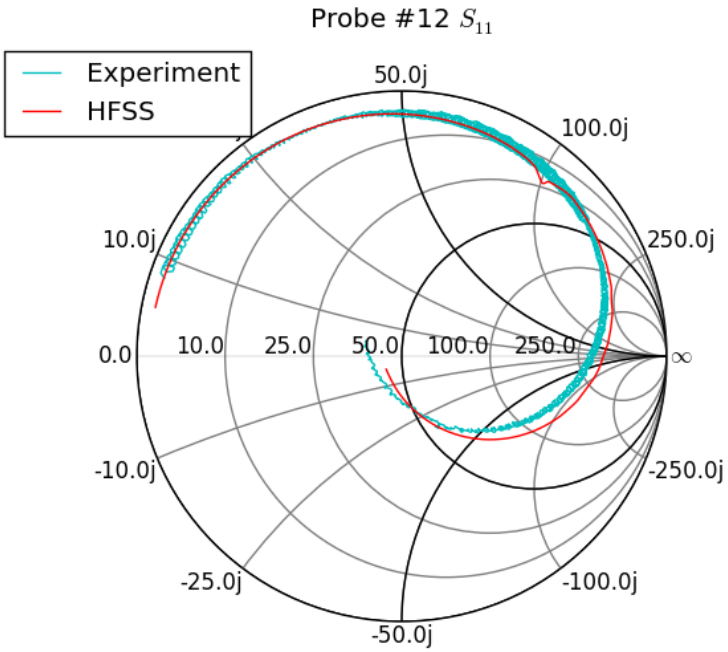

Figure 4.15: Probe position #12 HFSS-simulated S_{11} data versus experimental data.

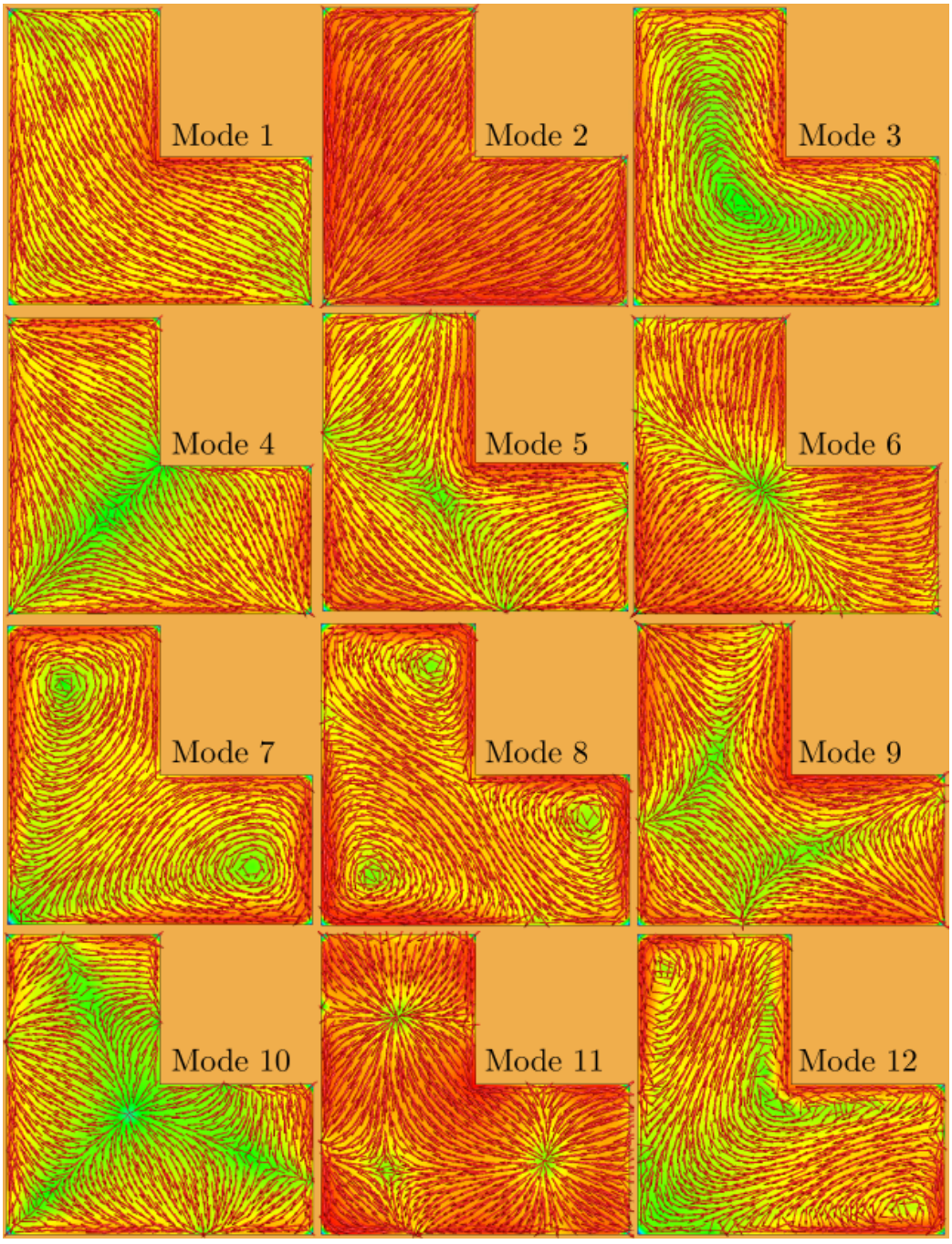

Figure 4.16: The first 12 modes at 2.0 GHz for the L-patch virtual probe model; all of these were deemed valid and used in the calculations. Current vectors' magnitudes are plotted on a decibel scale for ease of visualization.

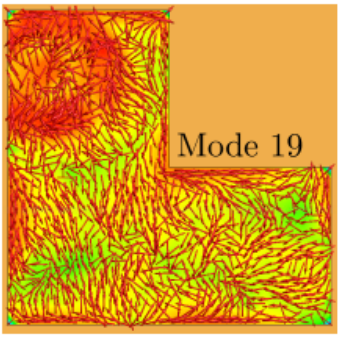

Figure 4.17: One of the discarded "scrambled" modes at 2.0 GHz for the virtual probe model.

Table 4.2: Details for the regular 3D grid of sampled electric field near-field values. The values at these points were linearly interpolated as needed for the virtual probe model computations.

Dimension	Start [mm]	Stop [mm]	Step [mm]	Count
$\hat{x}$	1.0	11.5	1.5	8
$\hat{y}$	1.0	23.5	1.5	16
$\hat{z}$	0.0	4.0	0.4	11

based on lossless (PEC) material, such an increase in frequency is actually somewhat expected: losses tend to reduce resonant frequencies. To quantify this frequency scaling, the TCM virtual probe data were interpolated, and a least-squares fit performed to minimize the difference between the experimental input resistance and frequency-scaled virtual probe input resistance data. Though the frequency scaling factors weren't constant with probe position (nor was any simple pattern discernible), using the average value for this fit gave reasonable results.

The second, more significant issue was the accuracy of the estimated input reactance. Even with the applied frequency scaling, the input reactance showed substantial error at the lower frequencies. For example, for probe position #0, the experimental data showed $X_{in} \approx 0\,\Omega$, while the virtual probe data gave $X_{in} \approx 80\,\Omega$. Since the virtual probe model doesn't explicitly model the behavior of the feed probe, errors of this sort were expected. As the input reactance data was consistently too inductive at low frequencies, with errors decreasing with increasing frequency, a natural solution was to see if a capacitor (modeling the feed's effects) in series with the input impedance would correct these errors. Again, a least-squares fit of the data was done to

investigate this possibility. Adding a capacitance did improve the lower frequencies' data, but at the expense of making the higher frequencies slightly too capacitive. Going just one step farther, a least-squares fit including both a series capacitor and a series inductor (along with the required frequency scaling) was done. This time, the input reactance data for the virtual probe model showed surprisingly good agreement. Much like the frequency scaling factor as a function of probe position, the required capacitances and inductances were neither constant nor easily predictable. The average values that were thus used for the data transform were a frequency scaling factor of 0.924, an inductance of 1.37 nH, and a capacitance of 0.729 pF.

As with the HFSS data, plots for probe positions #0 and #12 are given. Figure 4.18 compares input impedances for position #0, while Figure 4.19 compares input reflection coefficients on a Smith chart. Figures 4.20 and 4.21 likewise compare these quantities for probe position #12. In all of the plots, the "average fit" for the virtual probe model refers to applying the position-averaged frequency scaling and adding the position-averaged series reactances discussed above. While these corrections do substantially improve the input impedance estimate (compared to the "raw", or uncorrected data), the plots show that significant deviations still exist.

4.4.3 Wire Probe Model

Moving from the virtual to wire probe model, an increase in accuracy is expected due to the slight improvement in model accuracy, and indeed this ends up being the case. As with the previous model, the first 12 most significant modes at each frequency were used for the modeling. As an example, Figure 4.22 shows these at 2.0 GHz for probe position #19. Comparing to the first few modes of the virtual probe model in Figure 4.16, it becomes readily apparent that the feed probe *does* substantially alter the modes. Modes 2, 3, 4, and 6 for the wire probe model correspond to modes 1, 2, 3, and 4 of the virtual probe model, respectively. Interestingly, the wire probe model exhibits as its most significant mode (at least for this frequency) a CM with currents originating from the feed probe and spreading radially outward; such a mode has no counterpart among the significant modes of the other model. This helps to show why computing CMs of an unfed structure and

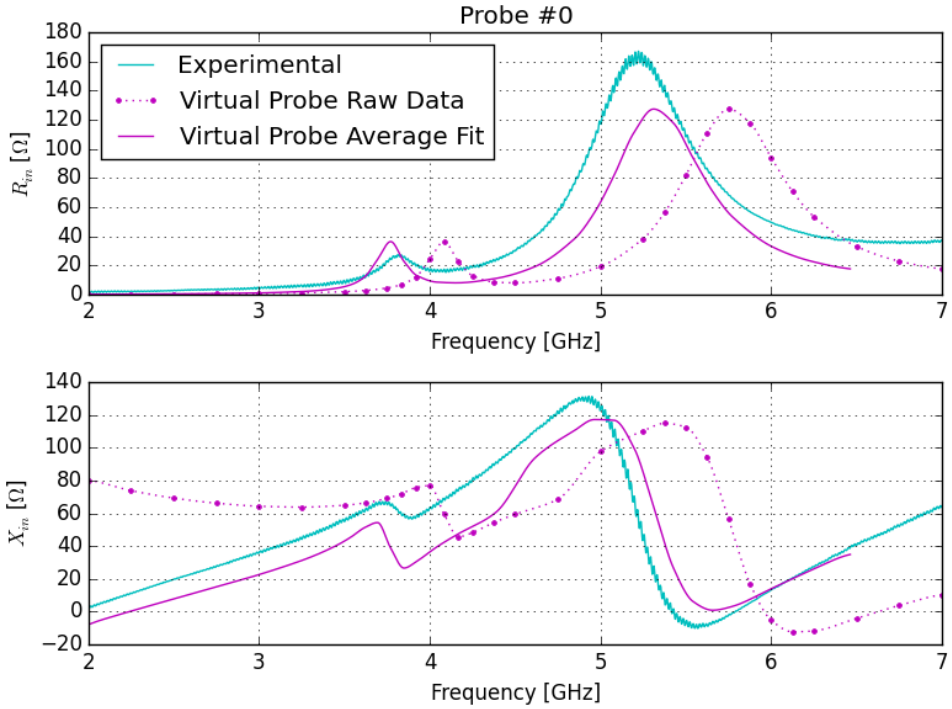

Figure 4.18: Probe position #0 input resistance and reactance for the virtual probe model data versus experimental data. The points on the raw data plot denote simulated frequencies.

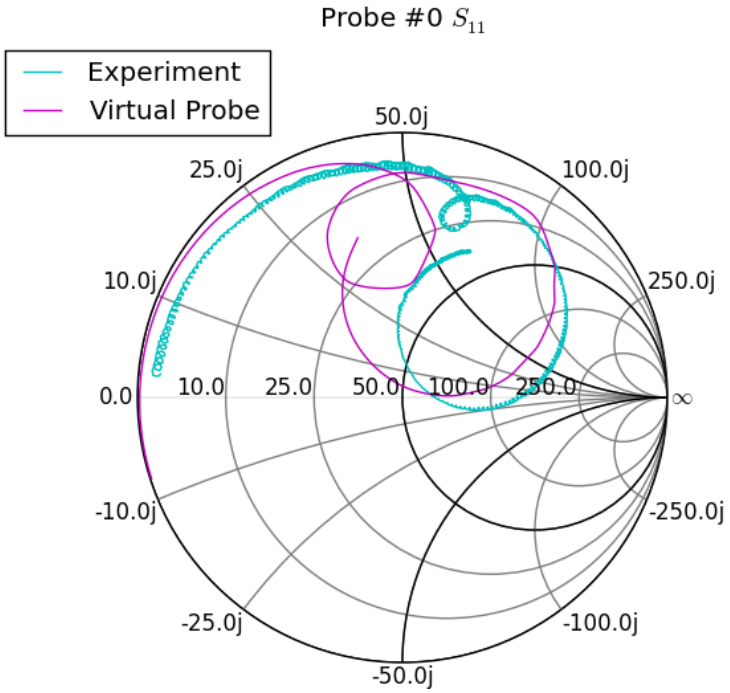

Figure 4.19: Probe position #0 virtual probe model S_{11} data versus experimental data.

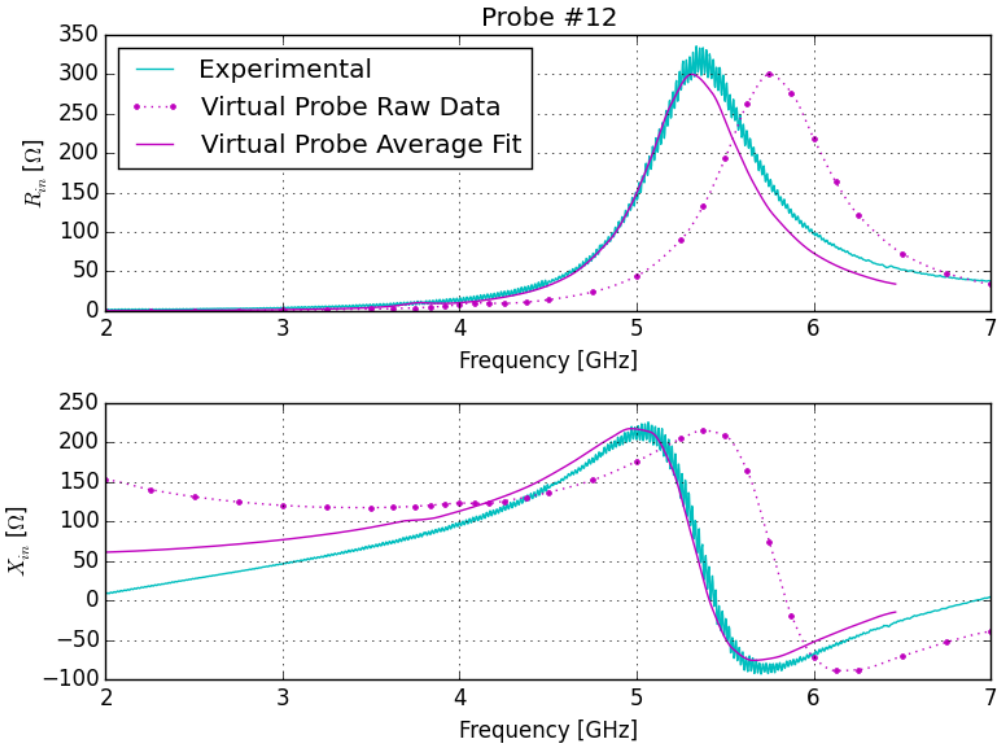

Figure 4.20: Probe position #12 input resistance and reactance for the virtual probe model data versus experimental data. The points on the raw data plot denote simulated frequencies.

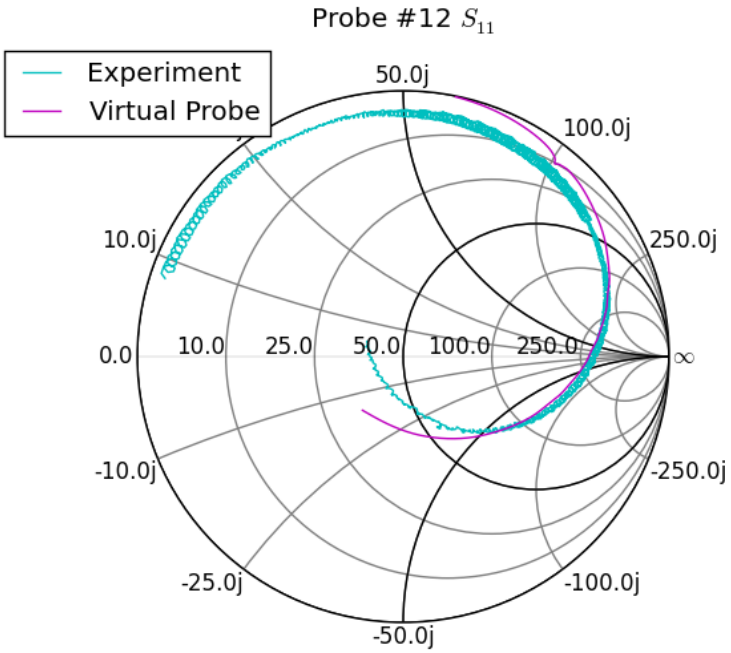

Figure 4.21: Probe position #12 virtual probe model S_{11} data versus experimental data.

later adding a feed is not a great idea. The implicit assumption that the feed doesn't alter the CMs is clearly not valid, as evidenced by this particular example.

Regarding the accuracy of the calculated input impedances, a scaling down in frequency of the wire probe data is needed, same as for the virtual probe model, to compensate for the model's lossless materials when compared to experimental data. A least-squares fit for this frequency scaling factor gives an average value of 0.922, strikingly close to the value of 0.924 for the virtual probe model. This model, however, requires no additional compensation. Shown in Figures 4.23 and 4.24 are the input impedance and S_{11} data for probe position #0, and the same for position #12 in Figures 4.25 and 4.26.

4.4.4 Comparison of Methods

With the decent accuracy of the two TCM-based methods established (albeit with a few necessary adjustments), a comparison of the two will now be examined. As far as input resistance goes, both the virtual and wire probe models offer good estimates with only a simple scaling down in frequency. The fact that the position-averaged best-fit frequency scale factors for both methods are quite similar makes the attributed cause (PEC versus lossy materials) quite credible. Were the frequency shift primarily a consequence of the method or the modes' patterns, it seems unlikely that the two different approaches would have such similar shifts. Further statistical information about the frequency scaling factors is tabulated in Table 4.3. An interesting difference between the two models' input resistances is that the wire probe model always has a larger resistance. One possible explanation is that of feed probe radiation. Since the virtual probe model assumes that the probe doesn't radiate, its losses due to radiation (which the input resistance captures) should be smaller. Furthermore, the assumption of no feed radiation is contingent upon the electrical length of the feed. As the frequency increases, the probe should begin to radiate more. Observing that the difference between the virtual and wire probe models' input resistances generally increases with frequency suggests that this is at least part of the explanation.

Using just the position-averaged fits (as opposed to the better, though unpredictable position-dependent ones), the wire probe model's input reac-

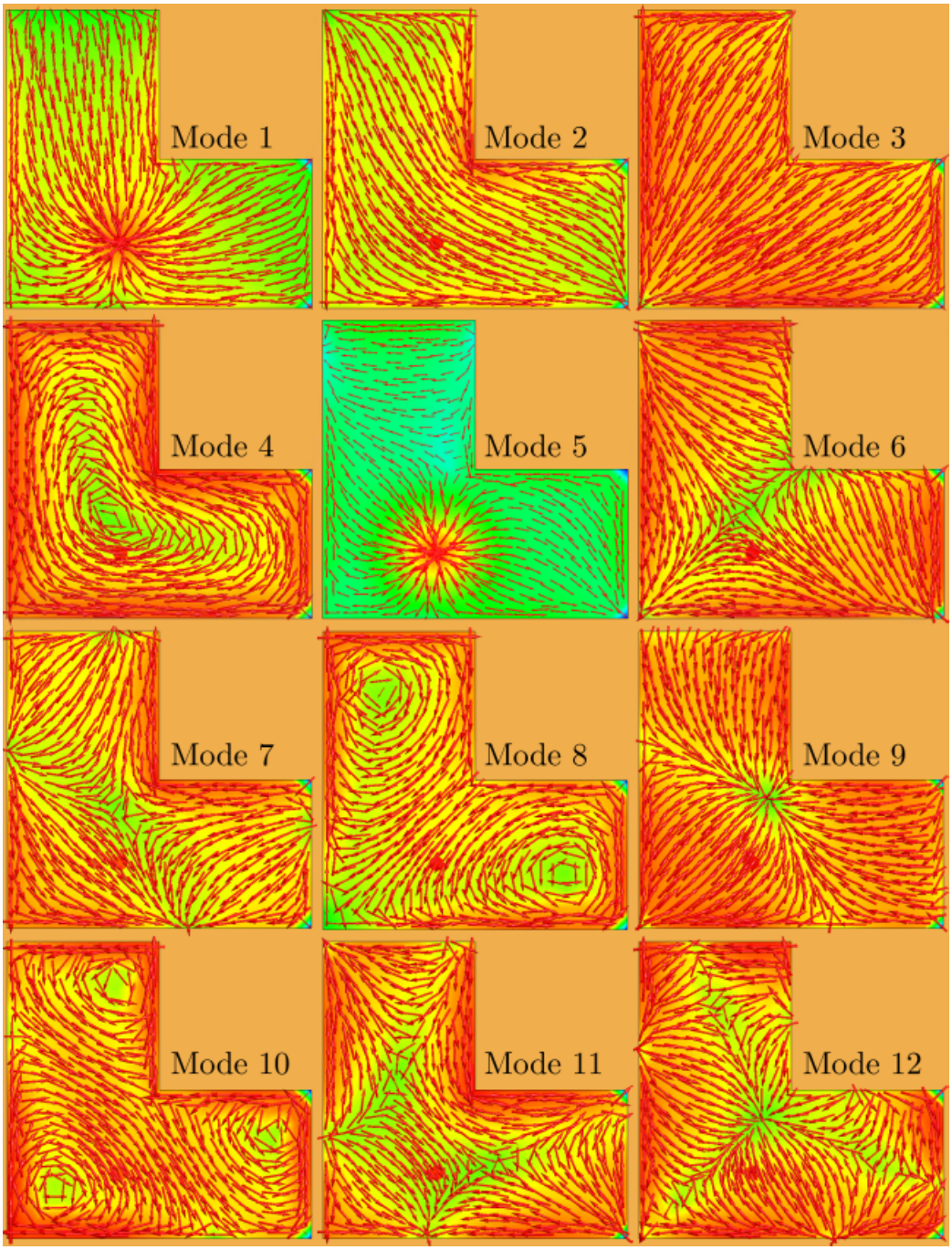

Figure 4.22: Modes at 2.0 GHz for the L-patch wire probe model, with the probe in position #19. Current vectors' magnitudes are plotted on a decibel scale for ease of visualization.

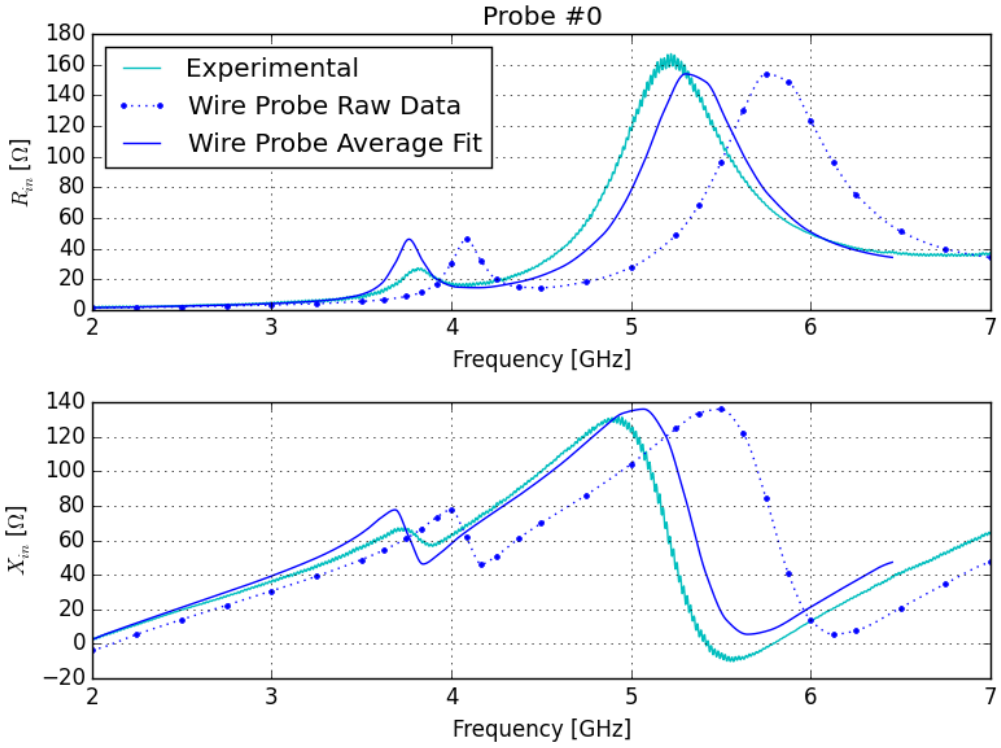

Figure 4.23: Probe position #0 input resistance and reactance for the wire probe model data versus experimental data. The points on the raw data plot denote simulated frequencies.

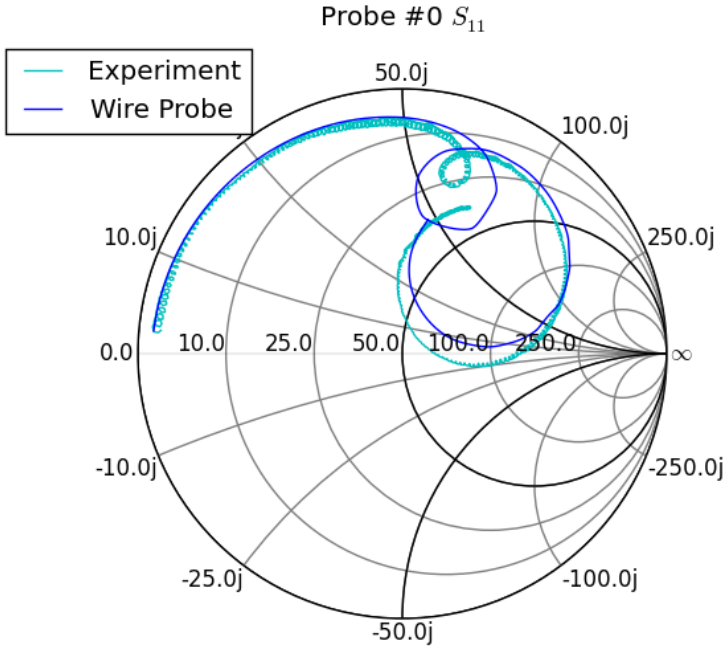

Figure 4.24: Probe position #0 wire probe model S_{11} data versus experimental data.

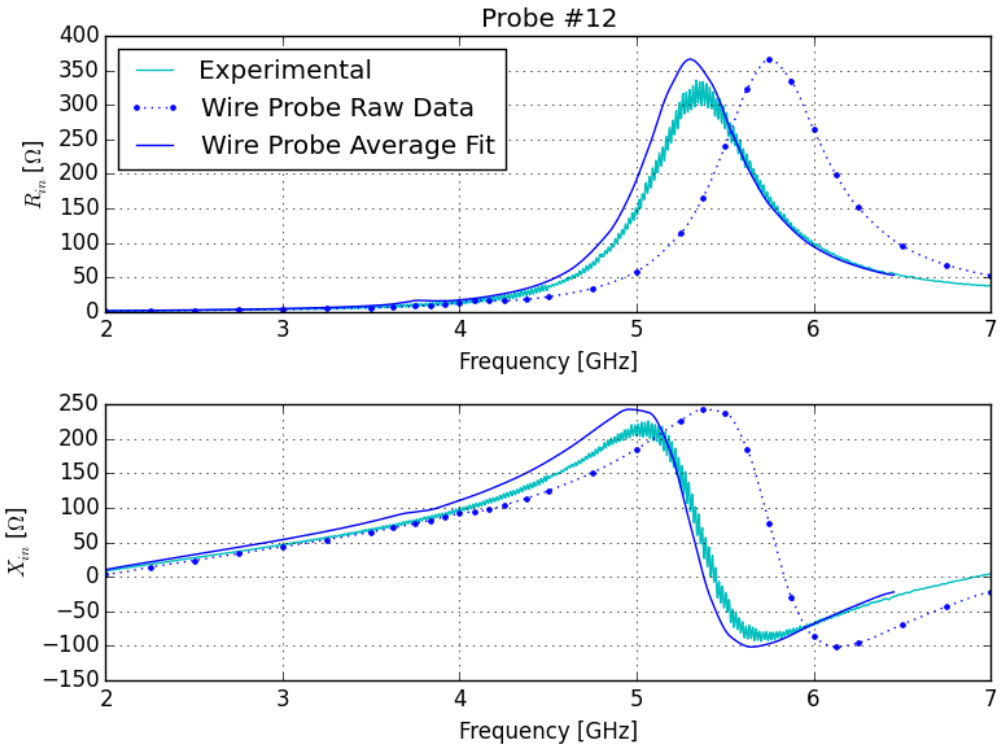

Figure 4.25: Probe position #12 input resistance and reactance for the wire probe model data versus experimental data. The points on the raw data plot denote simulated frequencies.

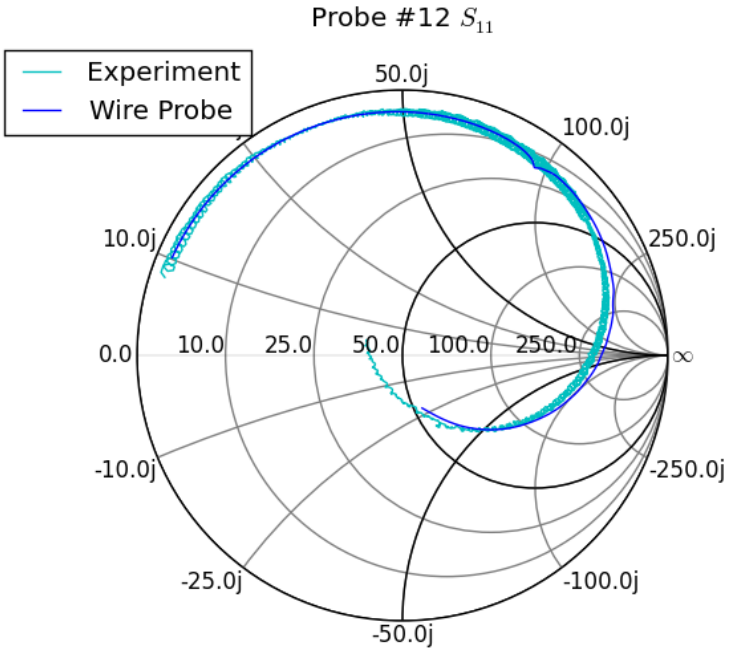

Figure 4.26: Probe position #12 wire probe model S_{11} data versus experimental data.

Table 4.3: Data statistics for the least-squares, best-fit compensation parameters as computed for both methods at the 21 different feed probe positions.

Method	Parameter	Average	Standard Deviation	Minimum	Maximum
Virtual Probe	L [nH]	1.37	0.255	0.768	2.04
Virtual Probe	C [pF]	0.792	0.240	0.324	1.17
Virtual Probe	Freq. Scaling	0.924	0.00860	0.906	0.941
Wire Probe	Freq. Scaling	0.922	0.00921	0.903	0.942

tance is typically better overall than the virtual probe's. Granted, the more accurate model is also the one giving more accurate results, which is to be expected. Given a relatively straightforward method to predict the virtual probe model's series reactive loading as a function of position (for a general MSA), the virtual probe method could become a viable alternative. As an example, Figure 4.27 shows the input impedance data for the two methods using each one's best-fit data at position #3; the two methods, while not perfect, do compare favorably. As a final set of comparisons, the estimated input impedances for probe positions #19 and #20 for all three simulation methods are given in Figures 4.28 and 4.29, where the TCM-based data are compensated with the position-averaged fits. While none of the methods exactly predict the input impedance over the entire range of frequencies, the general trends are correct. An important observation is that the HFSS-data does differ substantially in some places from the experimental data. This suggests that additional, unmodeled factors (such as those listed earlier in Section 4.4.1) are present in the real-world design. Either eliminating those differences in the real antenna (where possible), or more accurately modeling them in simulations would likely improve the accuracy of all three simulation methods.

4.4.5 Impedance Maps

Given that the wire probe model with its position-averaged frequency scaling factor compares fairly well to experimental data, this model should also be capable of generating reasonably accurate impedance maps. To that purpose, input impedances were calculated over frequency at a regular grid of feed probe positions, using the same model and simulation settings as for

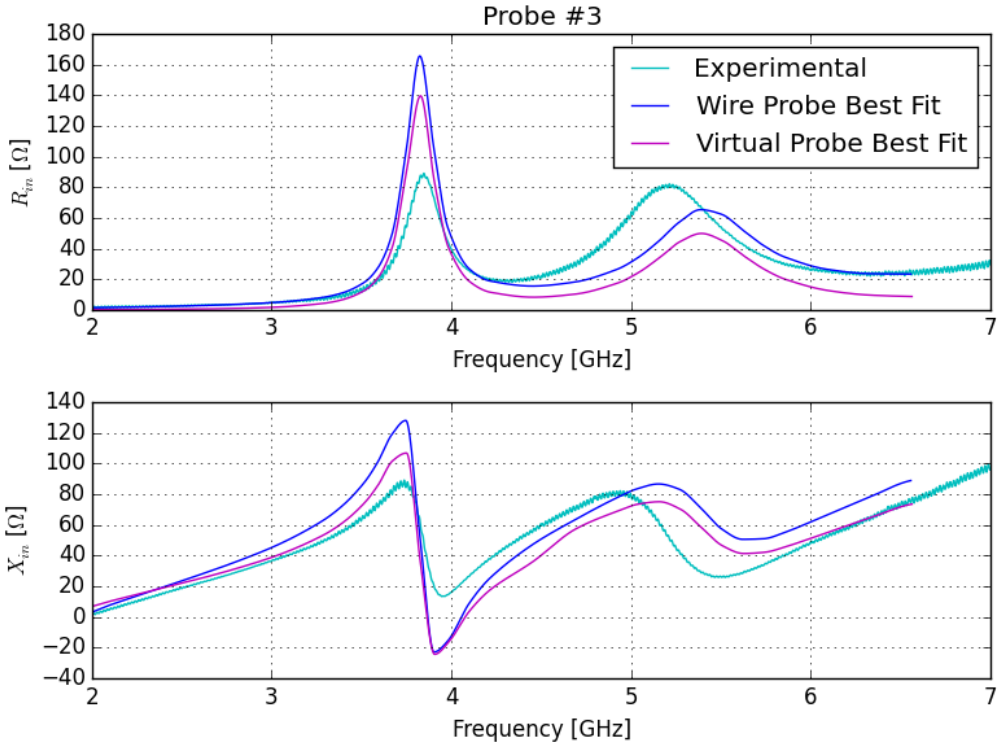

Figure 4.27: Input impedance for the two TCM-based methods for probe position #3. For this plot, the virtual probe model has been scaled in frequency by a factor of 0.938 and series-loaded with 1.44 nH in series with 0.664 pF, while the wire probe model has been scaled in frequency by 0.937.

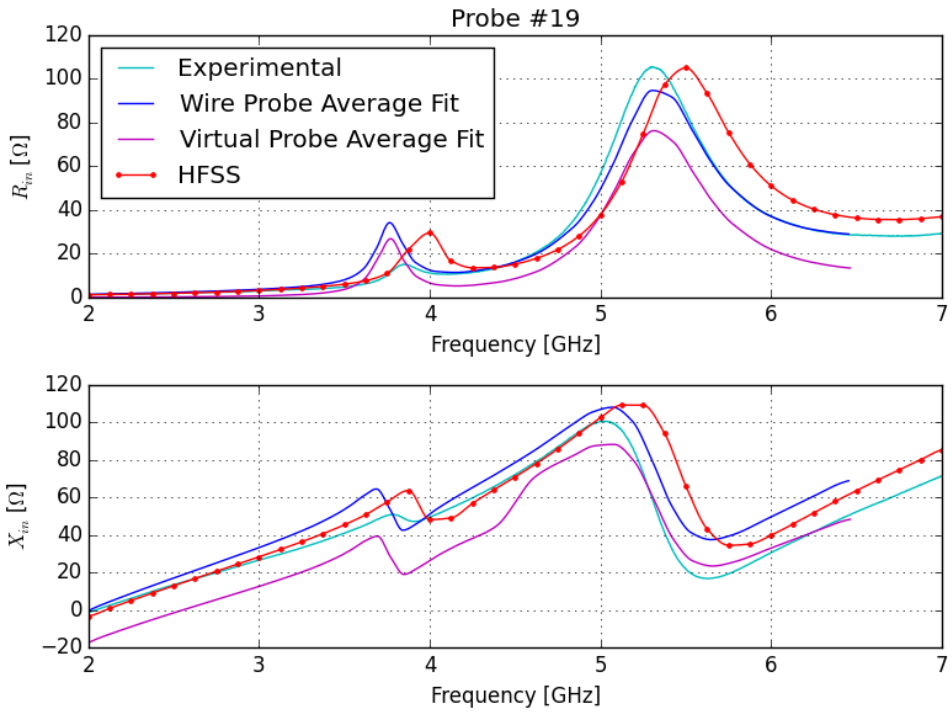

Figure 4.28: Comparison of input impedance data for probe position #19.

the experimental probe positions. The samples lay on an 8 by 16 grid, corresponding to the $\hat{x}$ and $\hat{y}$ sample points used earlier for the virtual probe model's field samples (Table 4.2); no points were sampled for $x \geq 12.5\,\text{mm}$ since this region's information may be obtained by symmetry. Impedance maps at 3.0 GHz and 6.0 GHz were then generated using HFSS-generated data (Figures 4.30 and 4.32) and wire probe model data (Figures 4.31 and 4.33), with the wire probe data scaled in frequency by the experimental position-averaged factor of 0.922. For both frequencies, the same scale is used to plot the maps of both methods for ease of comparison.

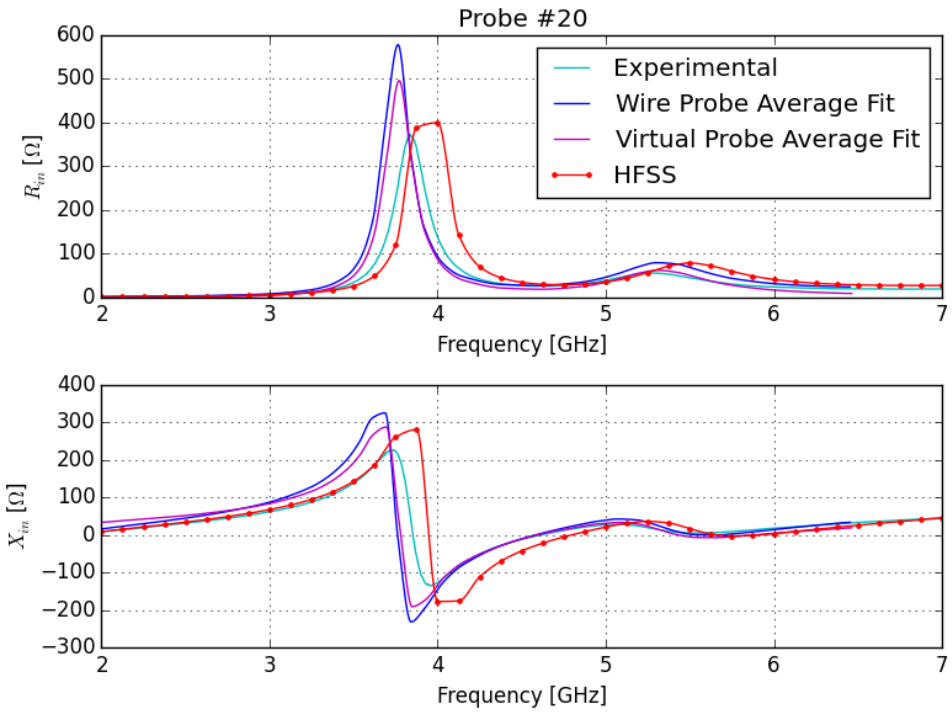

Figure 4.29: Comparison of input impedance data for probe position #20. The fact that the HFSS data doesn't seem to overestimate the input resistance near 4 GHz is more likely due to the interpolation method.

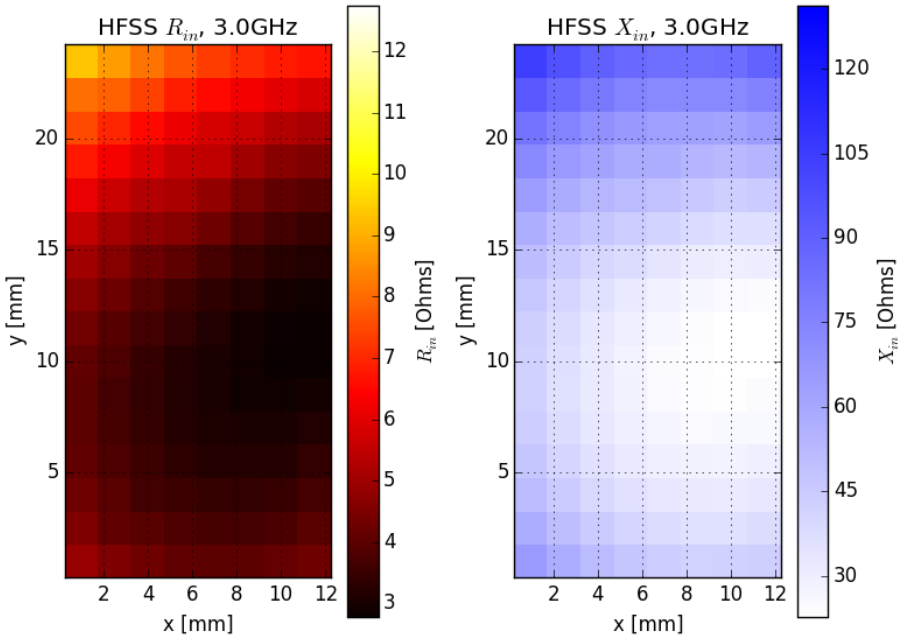

Figure 4.30: Input impedance maps at 3.0 GHz for the left-hand side of the L-patch using HFSS-generated data.

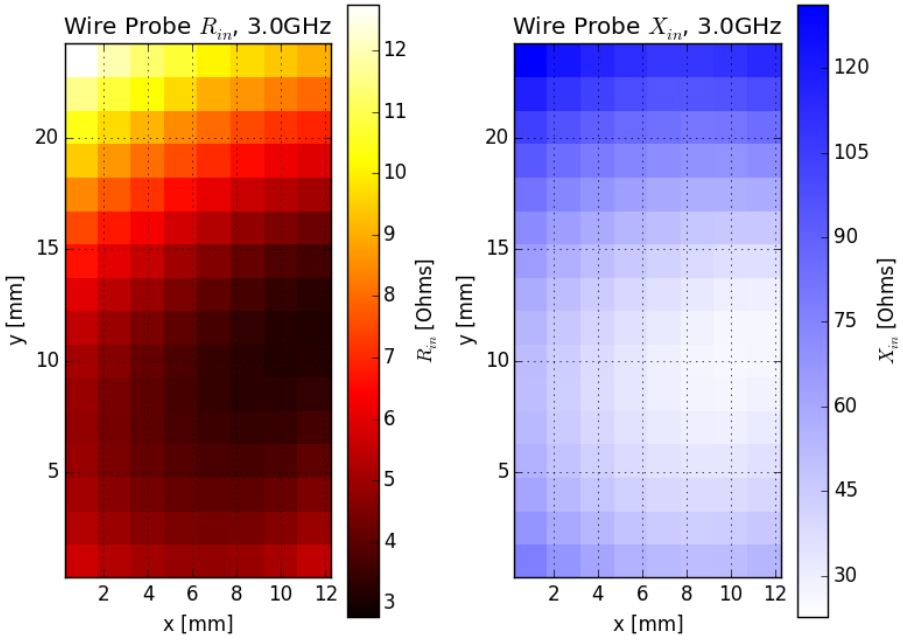

Figure 4.31: Input impedance maps at 3.0 GHz for the L-patch using wire probe model data.

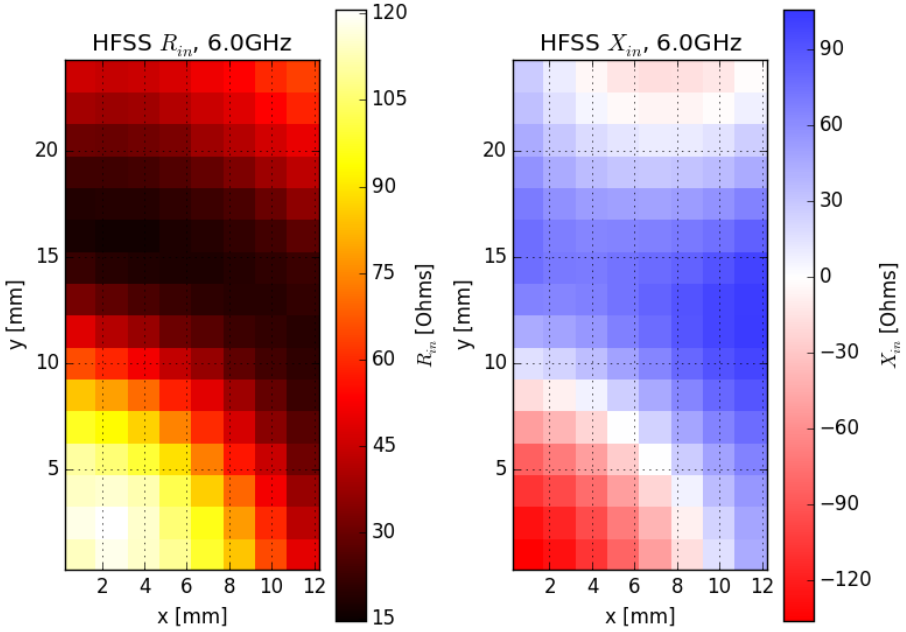

Figure 4.32: Input impedance maps at 6.0 GHz of the L-patch using HFSS-generated data.

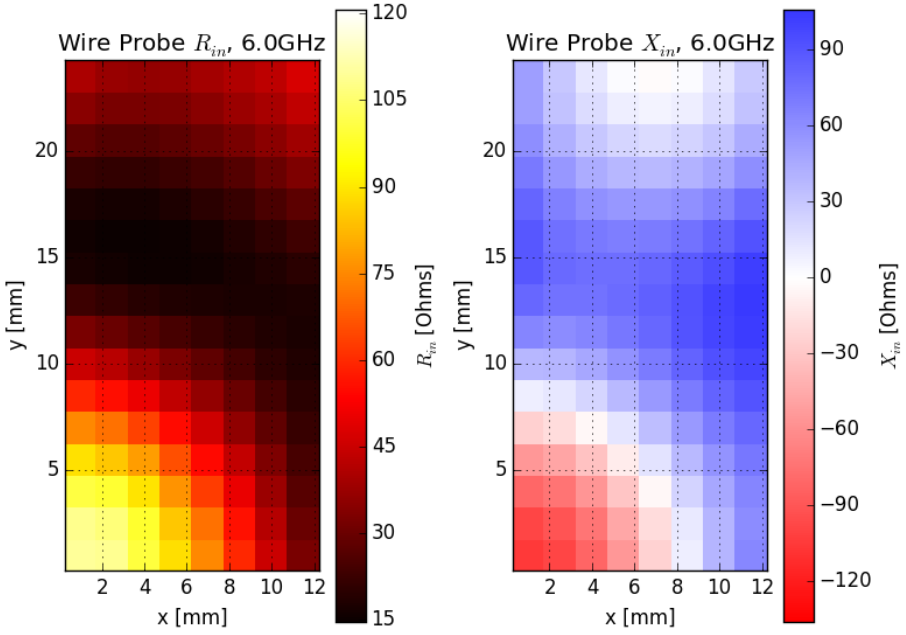

Figure 4.33: Input impedance maps at 6.0 GHz of the L-patch using wire probe model data.

CHAPTER 5

CONCLUSIONS

Two different methods for input impedance estimation were developed based on the theory of characteristic modes. An evaluation of their accuracy for a particular case study was performed, yielding good results and some important observations. Given the promising nature of these methods, a number of areas needing more research will be offered.

5.1 Implications of Results

Primarily based on the results of the case study of Chapter 4, a number of important implications for the use of TCM may be drawn. First and foremost, accurate modeling of the antenna feed probe for MSAs is important, especially if input reactance data is needed. Whether this modeling is done directly (via the wire probe model) or indirectly (via series reactive loading in the virtual probe model) isn't quite as critical, as both are better than no feed model. Ultimately, the required accuracy of the input impedance should specify the model: in designs where this parameter is more important, a better model should be used.

Secondly, the differences in input resistance between the two methods suggest that feed probe radiation isn't always negligible. Over the measured range of 2.0 GHz to 7.0 GHz, the 4.0 mm feed for the studied L-patch MSA ranged in electrical length from around $\lambda/37$ to $\lambda/10$. Even though all these lengths lie in a range that's fairly short relative to a wavelength, the MSA probe's radiation appears to be noticeable. One possible explanation for this is the loading nature of the MSA's patch. Much like a "top-hat" loaded monopole or an inverted-L antenna (ILA), the patch serves to extend the path along which current can flow, improving the radiation efficiency of the short, vertical wire segment – in this case, the feed probe.

A third implication of significant importance is the influence of the feed structure on an antenna's CMs. Much of the current literature on antenna design using TCM (more accurately, inspired by TCM) computes the CMs of a structure without a feed. Based on which modes radiate in the desired fashion, locations on the antenna are chosen to best couple to the selected modes. A feeding structure is then attached at one of those locations and the results inspected. For certain antenna feeds and/or antenna geometries, this approach will probably give good results. Applied more generally (or to MSAs), however, such an approach isn't likely to work. As shown for the L-patch MSA analyzed, the presence or absence of the feed probe can substantially alter the significant CMs of an antenna, even resulting in entirely new modes appearing. Although it was shown that the input impedance without a physical probe model in the simulations (*i.e.* the virtual probe model) could be compensated for with suitable series reactive loading, other antenna parameters are likely to be less forgiving. Antenna far-field radiation patterns, for instance, may prove to be more sensitive to the actual modes used. This work helps to stress the importance of accurately accounting for an antenna's structure when using TCM.

5.2 Future Work

Many interesting possibilities exist for future research based on this work. As stated early on, the use of CMs in this thesis was largely just because they offered a convenient, whole-domain set of basis functions for the current on an antenna. This means that many of the unique properties of CMs have yet to be leveraged. For example, analyzing a modal impedance map of the antenna could offer ways to select a feed position that optimally excites certain modes and not others, or that has certain far-field radiation pattern properties. Regarding the modes' radiation patterns, future work also includes investigating the accuracy of the radiated far field as computed by the weighted sum of modal far fields.

More broadly, research on implementing TCM for magneto-dielectric bodies would be of great value. One of the severe limitations of the virtual and wire probe models developed in this thesis is their present restriction to antennas composed exclusively of PEC. Very few real-world MSAs fall into this

category due to the fabrication challenges and fragility of such designs. With a better understood generalization of TCM to arbitrary materials, a much larger class of antennas could be analyzed. This potentially could lead to greater (or alternative) insights into the operation of more antennas, as well as better methods for systematic antenna design.

From a more mathematical or computational angle, research into methods to accelerate the wire probe model would be quite beneficial. As it currently is implemented, the impedance matrix for the antenna must be fully recomputed and the TCM generalized eigenvalue problem fully solved for every feed point simulated. This is computationally rather costly. Finding either mathematical methods or computational tricks to reduce this cost would make approaches such as high-resolution impedance maps a more feasible antenna design tool. Possible ways of accelerating this method could involve eigenvector and eigenvalue perturbation techniques, in which the feed position is only changed in small increments for which the CMs could be reliably updated.

These are only a few potential areas of future research, but doubtlessly many more exist. Research on TCM has only recently begun to accelerate and become more mainstream within the field of antenna design. As TCM is more widely accepted and more fully researched, many more design approaches based on this theory are expected to arise. The work developed in this thesis and the results offered by it should help offer useful insights and important implications for the development of such approaches.

APPENDIX A

CALCULATION OF CHARACTERISTIC MODES

Although the commercial method of moments solver FEKO provides many nice features and is itself capable of calculating CMs, its functionality is still somewhat constrained, especially for researching and developing TCM-based methods. Consequently, for all of the work in this thesis, FEKO was simply used to easily generate a structure's $\mathbf{Z}$ matrix and to later display its CMs. Actual calculating and working with the modes was instead done with custom Python scripts, to be detailed here.

After a PEC structure has been modeled in FEKO, one must next properly configure the FEKO simulation. Firstly, the frequencies of interest must be selected, then the structure meshed relatively densely. In practice, restricting the triangular mesh elements' largest sides to be at most anywhere between $\lambda/20$ and $\lambda/30$ at the highest frequency seems to provide good results. Though perhaps not strictly necessary, FEKO's solver should be set to store data in double precision (instead of the default single precision). In order to generate the necessary files, the solver must also be set to save its "matrix elements" (the $\mathbf{Z}$ matrix) to a `*.mat` file. If one desires to visualize the calculated CMs in FEKO, the solver must be set to save its currents to a `*.str` file, if such a file doesn't exist, and to read currents from such a file if it does exist. As part of the simulation setup, one must generate a request for surface currents, as well as create a plane wave source of zero magnitude (because CMs are excitation independent, so no active sources can be present). Adding the plane wave is theoretically not needed, however without it, FEKO won't generate and output a $\mathbf{Z}$ matrix. If one wishes to later view and quickly compare multiple CMs, the plane wave should be set to "loop over multiple directions"; doing so creates additional space in the current vector file (`*.str`) where multiple modes' eigencurrents can be later saved.

Once FEKO has been run and the impedance matrix generated, it may

be read in from the project's corresponding `*.mat` file. The data in this file is stored in binary format, documented on FEKO's website. One important point to note: for unknown reasons, FEKO stores this matrix in negated form. That is, after importing it, one must multiply all of the matrix entries (both real and imaginary parts) by -1:

$$\mathbf{Z} = -\mathbf{Z}_{imported} \tag{A.1}$$

Calculation of the CMs and their eigenvalues may be done by directly solving the generalized eigenvalue problem (equation 2.5), say with the SciPy's `scipy.linalg.eig` routine. This approach seems to work well enough, but tends to be slow. Although $\mathbf{Z}$ is supposed to be symmetric and $\mathbf{R}$ is supposed to be positive semidefinite, neither property holds in practice due to a combination of numerical error and the particular method of moments algorithm used by FEKO. Consequently, generalized eigenvalue solvers exploiting symmetry and positive (semi)definiteness (like `scipy.linalg.eigh`) can't be used to accelerate solving. A faster approach is the original method described by Harrington and Mautz [4] and briefly recreated here for completeness. Prior to applying Harrington and Mautz's method, which assumes $\mathbf{Z}$ is symmetric, FEKO's impedance matrix must be coerced to truly be symmetric (instead of very nearly so), say by averaging:

$$\mathbf{Z}_{symm} = \frac{1}{2}\left(\mathbf{Z} + \mathbf{Z}^T\right) \tag{A.2}$$

As detailed in [4], one first must diagonalize $\mathbf{R} = \mathrm{Re}[\mathbf{Z}_{symm}]$

$$\boldsymbol{\mu} = \mathbf{U}^T\mathbf{R}\mathbf{U} = \begin{bmatrix} \mu_1 & 0 & 0 & \cdots \\ 0 & \mu_2 & 0 & \cdots \\ 0 & 0 & \mu_3 & \cdots \\ \vdots & \vdots & \vdots & \ddots \end{bmatrix} \tag{A.3}$$

where $\boldsymbol{\mu}$ is the diagonal matrix of $\mathbf{R}$'s eigenvalues μ_i and $\mathbf{U}$ is the orthogonal matrix whose columns are eigenvectors of $\mathbf{R}$. Because $\mathbf{R}$ is symmetric and supposed to be positive semidefinite, all of its eigenvalues should be nonnegative. In practice this isn't the case. For the matrices used in this thesis, generally about half of $\mathbf{R}$'s eigenvalues had negative (though small) real components. While Harrington and Mautz suggest zeroing all of the eigenvalues

$\mu_i < M\mu_1$ for some threshold M (such as 10^{-3}) relative to the largest eigenvalue μ_1, all of the eigenvalues with positive real components were kept for this work. With this zeroing, the matrix $\boldsymbol{\mu}$ can be block-partitioned (sorting and rearranging the eigenvalues as necessary) as

$$\boldsymbol{\mu} = \begin{bmatrix} \boldsymbol{\mu}_{11} & \mathbf{0} \\ \mathbf{0} & \mathbf{0} \end{bmatrix} \tag{A.4}$$

The matrix $\mathbf{A}$ is then formed and partitioned in the same manner as $\boldsymbol{\mu}$, where $\mathbf{X} = \mathrm{Im}[\mathbf{Z}_{symm}]$:

$$\mathbf{A} = \mathbf{U}^T\mathbf{X}\mathbf{U} = \begin{bmatrix} \mathbf{A}_{11} & \mathbf{A}_{12} \\ \mathbf{A}_{21} & \mathbf{A}_{22} \end{bmatrix} \tag{A.5}$$

Due to symmetry, $\mathbf{A}_{12}^T = \mathbf{A}_{21}$. By forming the matrix $\mathbf{B}$ as will follow, the generalized eigenvalue problem is finally cast into a standard (unweighted) eigenvalue problem. Taking the reciprocal square root of the diagonal entries of $\boldsymbol{\mu}_{11}$ and denoting the result as $\boldsymbol{\mu}_{11}^{-1/2}$,

$$\boldsymbol{\mu}_{11}^{-1/2} = \begin{bmatrix} \mu_1^{-1/2} & 0 & 0 & \cdots \\ 0 & \mu_2^{-1/2} & 0 & \cdots \\ 0 & 0 & \mu_3^{-1/2} & \cdots \\ \vdots & \vdots & \vdots & \ddots \end{bmatrix} \tag{A.6}$$

let

$$\mathbf{B} = \boldsymbol{\mu}_{11}^{-1/2}\left(\mathbf{A}_{11} - \mathbf{A}_{12}\mathbf{A}_{22}^{-1}\mathbf{A}_{12}^T\right)\boldsymbol{\mu}_{11}^{-1/2} \tag{A.7}$$

The resulting eigenequation

$$\mathbf{B}\vec{y} = \lambda\vec{y} \tag{A.8}$$

has the same eigenvalues λ as the original problem, and eigenvectors $\vec{y}$ that may be transformed into the CM's eigenvectors using

$$\vec{J}_n = \mathbf{U}\begin{bmatrix} \mathbf{1} \\ -\mathbf{A}_{22}^{-1}\mathbf{A}_{12}^T \end{bmatrix}\boldsymbol{\mu}_{11}^{-1/2}\vec{y} \tag{A.9}$$

Once the CMs $\vec{J}_n$ have been calculated, they next need to be normalized to radiate unit power, per the relation of Equation 2.7. For this work, the eigen-

vectors were normalized against the positive-semidefinite-coerced $\mathbf{R}$ matrix,

$$\hat{\mathbf{R}} = \mathbf{U} \begin{bmatrix} \boldsymbol{\mu}_{11} & \mathbf{0} \\ \mathbf{0} & \mathbf{0} \end{bmatrix} \mathbf{U}^H \tag{A.10}$$

The conjugate-transpose of $\mathbf{U}$ is taken to ensure that any complex-valued components become purely real. Using the conjugate form of the normalization to compute the (unnormalized) mode's radiated power,

$$P_n = \langle \vec{J}_n^*, \hat{\mathbf{R}} \vec{J}_n \rangle \tag{A.11}$$

the given mode $\vec{J}_n$ is then normalized as

$$\hat{\vec{J}}_n = \frac{\vec{J}_n}{\sqrt{P_n}} \tag{A.12}$$

The conjugate form in equation A.11 is used so that any small imaginary components in the eigenvectors (from numerical inaccuracies) are canceled out, giving purely real P_n values.

At this point, the CMs (eigenvectors) and their eigenvalues have been computed for the given structure at the given frequency. If multiple frequencies have been simulated, the $\mathbf{Z}$ matrix for each frequency may be processed in a like manner. (Note that for multiple frequencies, FEKO stores all of the impedance matrices in the same `*.mat` file.) If one wishes to visualize the CMs, compute their radiated far-fields, or perform other similar tasks, the computed eigenvectors may be written back into FEKO's `*.str` file. Provided FEKO has been configured to read data from this file (when it exists), re-running the FEKO simulation will set the eigenvectors as existing surface current densities, which may be visualized in POSTFEKO (the FEKO suite tool for viewing and plotting results).

REFERENCES

[1] R. J. Garbacz, "A generalized expansion for radiated and scattered fields," Ph.D. dissertation, Ohio State University, Columbus, OH, 1968.

[2] R. Garbacz and R. Turpin, "A generalized expansion for radiated and scattered fields," *IEEE Transactions on Antennas and Propagation*, vol. 19, no. 3, pp. 348 – 358, May 1971.

[3] R. Harrington and J. Mautz, "Theory of characteristic modes for conducting bodies," *IEEE Transactions on Antennas and Propagation*, vol. 19, no. 5, pp. 622 – 628, Sept. 1971.

[4] R. Harrington and J. Mautz, "Computation of characteristic modes for conducting bodies," *IEEE Transactions on Antennas and Propagation*, vol. 19, no. 5, pp. 629 – 639, Sept. 1971.

[5] R. F. Harrington, J. Mautz, and Y. Chang, "Characteristic modes for dielectric and magnetic bodies," *IEEE Transactions on Antennas and Propagation*, vol. 20, no. 2, pp. 194–198, Mar. 1972.

[6] Y. Chang and R. F. Harrington, "A surface formulation for characteristic modes of material bodies," *IEEE Transactions on Antennas and Propagation*, vol. 25, no. 6, pp. 789–795, Nov. 1977.

[7] EM Software & Systems - S.A. (Pty) Ltd, *FEKO Suite 6.3 (www.feko.info)*. 32 Techno Avenue, Technopark, Stellenbosch 7600, South Africa: EM Software & Systems - S.A. (Pty) Ltd, 2014.

[8] S. Rao, D. Wilton, and A. Glisson, "Electromagnetic scattering by surfaces of arbitrary shape," *IEEE Transactions on Antennas and Propagation*, vol. 30, no. 3, pp. 409–418, 1982.

[9] B. Austin and K. Murray, "The application of characteristic-mode techniques to vehicle-mounted NVIS antennas," *IEEE Antennas and Propagation Magazine*, vol. 40, no. 1, pp. 7–21, Feb. 1998.

[10] M. Capek, P. Hazdra, P. Hamouz, and J. Eichler, "A method for tracking characteristic numbers and vectors," *Progress In Electromagnetics Research B*, no. 33, pp. 115–134, 2011.

[11] K. R. Carver and J. Mink, "Microstrip antenna technology," *IEEE Transactions on Antennas and Propagation*, vol. 29, no. 1, pp. 2–24, Jan. 1981.

[12] G. Shaker, S. Safavi-Naeini, N. Sangary, and M. Bakr, "A generalized modal analysis method for antenna design," in *IEEE Antennas and Propagation Society International Symposium, 2009. APSURSI '09.*, June 2009, pp. 1–4.

[13] G. Shaker, "Circuit-theoretic physics-based antenna synthesis and design techniques for next-generation wireless devices," Ph.D. dissertation, University of Waterloo, Waterloo, Ontario, 2013.

[14] H. Chang-Hsiu and P. Hsu, "Effect of feed modeling on the evaluation of input impedance of microstrip antennas," *IEEE Transactions on Magnetics*, vol. 25, no. 4, pp. 3058–3060, July 1989.

[15] W. C. Chew, Z. Nie, and Y. T. Lo, "The effect of feed on the input impedance of a microstrip antenna," *Microwave and Optical Technology Letters*, vol. 3, no. 3, pp. 79–83, 1990.

[16] A. Yee and R. Garbacz, "Self- and mutual-admittances of wire antennas in terms of characteristic modes," *IEEE Transactions on Antennas and Propagation*, vol. 21, no. 6, pp. 868–871, Nov. 1973.

[17] J. Ethier and D. McNamara, "Antenna shape synthesis without prior specification of the feedpoint locations," *IEEE Transactions on Antennas and Propagation*, vol. 62, no. 10, pp. 4919–4934, Oct. 2014.

[18] K. A. Obeidat, B. D. Raines, and R. G. Rojas, "Discussion of series and parallel resonance phenomena in the input impedance of antennas," *Radio Science*, vol. 45, no. 6, 2010.

[19] M. Cabedo-Fabres, E. Antonio-Daviu, M. Ferrando-Bataller, and A. Valero-Nogueira, "On the use of characteristic modes to describe patch antenna performance," in *IEEE Antennas and Propagation Society International Symposium, 2003.*, vol. 2, June 2003, pp. 712–715.

[20] M. Cabedo-Fabres, E. Antonino-Daviu, A. Valero-Nogueira, and M. Bataller, "The theory of characteristic modes revisited: A contribution to the design of antennas for modern applications," *IEEE Antennas and Propagation Magazine*, vol. 49, no. 5, pp. 52 –68, Oct. 2007.

[21] J. Adams and J. Bernhard, "Broadband equivalent circuit models for antenna impedances and fields using characteristic modes," *IEEE Transactions on Antennas and Propagation*, vol. 61, no. 8, pp. 3985–3994, Aug. 2013.

[22] J. J. Adams, "Accelerated frequency interpolation of antenna impedances using characteristic modes," in *2014 IEEE Antennas and Propagation Society International Symposium (APSURSI)*, July 2014, pp. 1413–1414.

[23] D. M. Pozar, "Input impedance and mutual coupling of rectangular microstrip antennas," *IEEE Transactions on Antennas and Propagation*, vol. 30, no. 6, pp. 1191–1196, Nov. 1982.

[24] J. Eichler, P. Hazdra, and M. Capek, "Aspects of mesh generation for characteristic-mode analysis [EM programmer's notebook]," *IEEE Antennas and Propagation Magazine*, vol. 56, no. 3, pp. 172–183, June 2014.

[25] ANSYS® Electromagnetics Suite, Release 15.0, Help System, *Getting Started with HFSS^{TM}: A Dielectric Resonator Antenna*. ANSYS, Inc., 2013.

[26] scikit-rf Development Team, "scikit-rf : Open source RF engineering," 2009-present, http://www.scikit-rf.org.